INTERNATIONAL JOURNAL FOR NUMERICAL METHODS IN FLUIDS
Int. J. Numer. Meth. Fluids 2006; **50**:165–197
Published online 1 September 2005 in Wiley InterScience (www.interscience.wiley.com). DOI: 10.1002/fld.1049

On coupling the Reynolds-averaged Navier–Stokes equations with two-equation turbulence model equations

Seungsoo Lee*,†,§ and Dong Whan Choi‡,¶

Department of Aerospace Engineering, Inha University, Incheon, South Korea

SUMMARY

Two methods for coupling the Reynolds-averaged Navier–Stokes equations with the q–ω turbulence model equations on structured grid systems have been studied; namely a loosely coupled method and a strongly coupled method. The loosely coupled method first solves the Navier–Stokes equations with the turbulent viscosity fixed. In a subsequent step, the turbulence model equations are solved with all flow quantities fixed. On the other hand, the strongly coupled method solves the Reynolds-averaged Navier–Stokes equations and the turbulence model equations simultaneously. In this paper, numerical stabilities of both methods in conjunction with the approximated factorization-alternative direction implicit method are analysed. The effect of the turbulent kinetic energy terms in the governing equations on the convergence characteristics is also studied. The performance of the two methods is compared for several two- and three-dimensional problems. Copyright © 2005 John Wiley & Sons, Ltd.

KEY WORDS: Reynolds-averaged Navier–Stokes equations; two-equation turbulence model equations; von Neumann stability analysis; strongly coupled method; loosely coupled method

1. INTRODUCTION

The so-called density-based methods solve the continuity equation, the momentum equations, and the energy equation of the Navier–Stokes equations simultaneously. This is desirable since the Navier–Stokes equations are fully coupled through the convection terms. With the density-based methods, coupling of the two-equation turbulence model equations with the Reynolds-averaged Navier–Stokes equations can be done in two ways for the steady turbulent flow computations. One is the strongly coupled method [1–4] and the other is the loosely coupled method [5–7]. The former solves the Navier–Stokes equations and the turbulence model

*Correspondence to: Seungsoo Lee, Department of Aerospace Engineering, Inha University, Incheon, South Korea.
†E-mail: slee@inha.ac.kr
‡E-mail: dwchoi@inha.ac.kr
§Associate Professor.
¶Professor.

Contract/grant sponsor: Korea Science and Engineering Foundation; contract/grant number: R01-2003-000-10744-0

Received 31 May 2004
Revised 3 June 2005
Accepted 25 June 2005

equations simultaneously. On the other hand, the latter solves the Navier–Stokes equations and the turbulence model equations in sequence. While the strongly coupled method is preferred because of possible numerical stability gain with coupling of the Navier–Stokes equations and the turbulence model equations, the loosely coupled method is preferred because of relative simplicity in implementing the turbulence model equations into the existing Navier–Stokes solvers. Despite its significance, however, there seems to be no firm analytical basis on how to couple the Reynolds-averaged Navier–Stokes equations and the turbulence model equations.

Kunz and Lakshminarayana [1] studied numerical stabilities of an explicit Navier–Stokes code with the k–ε turbulence model equations. They argued that both coupling methods had the same linear stability characteristics when the explicit Runge–Kutta time stepping method was used. They also showed that actual convergence histories of both methods were the same by comparing the strongly coupled solver and the loosely coupled solver. Lui and Zheng [2] showed that a strongly coupled method for solving the Navier–Stokes equations and the k–ω turbulence model equations was far better than a loosely coupled method when using a multi-stage scheme. Residual smoothing and multi-grid method were applied for fast convergence. It seems that their results are somewhat contradictory to Kunz and Lakshminarayana's work. In Lui and Zheng's work, however, the multi-grid method was not applied to the k–ω equations for the loosely coupled method, while it was applied to both the Navier–Stokes equations and the k–ω equations for the strongly coupled method. This would change the convergence behaviour of the loosely coupled method completely. Recently, Barakos and Drikakis [3] compared the performance of three different coupling strategies for coupling the Navier–Stokes equations and the two-equation turbulence models (k–ε and k–ω models): an implicit coupled method, an implicit decoupled method and an explicit method. They showed that the implicit coupled method was superior to other coupling methods. Their implicit decoupled method, however, utilized the explicit Runge–Kutta time stepping method for the turbulence model equations and the implicit unfactored scheme for the Navier–Stokes equations, while the implicit coupled method utilized the implicit unfactored scheme for the flow equations and the turbulence model equations. Venkateswaran and Merkle [4] asserted that the strongly coupled method should be used if the turbulent kinetic energy contributions in the state equation and momentum equation were present, and that there would not be much to be gained by using the strongly coupled method when the turbulent kinetic energy contributions were ignored. However their arguments are based on speculations rather than on analysis or actual numerical experiments.

In 1990, Lee and Dulikravich [8] devised a stability analysis method for their incompressible magneto-hydrodynamic (MHD) solver. They adopted the four-stage Runge–Kutta time stepping method and the loosely coupled method to solve the incompressible Navier–Stokes equations and the magnetic transport equations. Their stability analysis starts by constructing the composite solution vector that is composed of the components of the solution vector of the Navier–Stokes equations and those of the magnetic field vector, and recognizing the loosely coupled method as a two-step method. The first step is to update the solution vector of the Navier–Stokes equations with the magnetic field vector kept constant, while the second step is to update the magnetic field vector with the solution vector of the Navier–Stokes equations kept constant. They showed that the stability of the loosely coupled method was ensured if the separate steps were stable.

In this paper, linear stability characteristics of the AF-ADI scheme have been analysed for both the strongly coupled method and the loosely coupled method for solving the Reynolds-

averaged Navier–Stokes equations and Coakley's q–ω turbulence model equations [9]. The standard vector stability analysis is made for the strongly coupled system, while Lee and Dulikravich's interpretation [8] is used for the stability of the loosely coupled system. Furthermore, the stability characteristics with and without the turbulent kinetic energy contributions in the state equation and the momentum equations are also studied. Two- and three-dimensional Navier–Stokes codes using both the strongly coupled method and the loosely coupled method are developed and applied to several turbulent flow test cases to validate the stability results.

2. GOVERNING EQUATIONS

The Reynolds-averaged Navier–Stokes equations for compressible flows in Cartesian tensor form are given by

$$\begin{aligned} \rho_{,t} + (\rho u_j)_{,j} &= 0 \\ (\rho u_i)_{,t} + (\rho u_i u_j - \sigma_{ij})_{,j} &= 0 \\ e_{,t} + (e u_j - u_i \sigma_{ij} + q_j)_{,j} &= 0 \end{aligned} \tag{1}$$

where $(\cdot)_{,t} = \partial/\partial t$, and $(\cdot)_{,j} = \partial/\partial x_j$; ρ is the density, u_j is the velocity vector and e is the total energy. The equation of state for the ideal gas relates the pressure with the total energy

$$e = \frac{p}{\gamma - 1} + \frac{1}{2}\rho u_i u_i + \rho k \tag{2}$$

where k is the turbulent kinetic energy and γ is the ratio of the specific heat. According to Boussinesq's eddy-viscosity hypothesis and Fourier's law, the stress tensor σ_{ij} and the heat flux vector q_j are expressed in terms of the velocity gradient tensor and the temperature gradient

$$\sigma_{ij} = \mu_T(u_{i,j} + u_{j,i} - \tfrac{2}{3}\delta_{ij}u_{k,k}) - (p + \tfrac{2}{3}\rho k)\delta_{ij}, \quad q_j = -k_T T_{,j} \tag{3}$$

The total viscosity and the total heat conductivity are defined by the sum of the molecular and turbulent ones

$$\mu_T = \mu_m + \mu_t, \quad k_T = k_m + k_t = C_p\left(\frac{\mu_m}{Pr} + \frac{\mu_t}{Pr_t}\right) \tag{4}$$

where Pr and Pr_t are the Prandtl number and the turbulent Prandtl number, respectively, and C_p is the specific heat at constant pressure.

If we define the turbulent pressure as suggested in References [4, 10]

$$p_t = p + \tfrac{2}{3}\rho k \tag{5}$$

then the Navier–Stokes equations and the state equation can be rewritten as

$$\begin{aligned} \rho_{,t} + (\rho u_j)_{,j} &= 0 \\ (\rho u_i)_{,t} + (\rho u_i u_j + p_t\delta_{ij} - \tau_{ij})_{,j} &= 0 \end{aligned} \tag{6}$$

$$e_{,t} + \{(e + p_t)u_j - u_i\tau_{ij} + q_j\}_{,j} = 0$$

$$e = \frac{p_t}{\gamma - 1} + \frac{1}{2}\rho u_i u_i + \frac{3\gamma - 5}{3(\gamma - 1)}\rho k \quad \text{or} \quad p_t = \rho RT + \tfrac{2}{3}\rho k \tag{7}$$

where the viscous stress tensor and the flux vector are defined by

$$\tau_{ij} = \mu_T(u_{i,j} + u_{j,i} - \tfrac{2}{3}\delta_{ij}u_{k,k}), \quad q_j = -k_T T_{,j} \tag{8}$$

The subscript in the turbulent pressure will be dropped for convenience.

2.1. Comments on governing equations

Some researchers [6, 7] ignore the turbulent kinetic energy contributions to the total energy, and the momentum equations. In this case, the Navier–Stokes equations and the state equation become

$$\begin{aligned} \rho_{,t} + (\rho u_j)_{,j} &= 0 \\ (\rho u_i)_{,t} + (\rho u_i u_j + p\delta_{ij} - \tau_{ij})_{,j} &= 0 \\ e_{,t} + \{(e + p)u_j - u_i\tau_{ij} + q_j\}_{,j} &= 0 \end{aligned} \tag{9}$$

$$e = \frac{p}{\gamma - 1} + \frac{1}{2}\rho u_i u_i \quad \text{or} \quad p = \rho RT \tag{10}$$

Notice that the difference between the two systems is in the state equation only. Moreover, the viscous stress tensor and the flux vector remain the same. If we define a flag, ζ as

$\zeta = 0$ if the turbulent kinetic energy contribution is ignored

$\zeta = 1$ if the turbulent kinetic energy contribution is included

then the combined state equation becomes

$$e = \frac{p}{\gamma - 1} + \frac{1}{2}\rho u_i u_i + \rho k\zeta C \quad \text{or} \quad p = \rho RT + \tfrac{2}{3}\rho k\zeta \tag{11}$$

where $C = (3\gamma - 5)/3(\gamma - 1)$.

One of successful two-equation turbulence models is Coakley's q–ω turbulence model [9]. This model uses the turbulent velocity scale q, and the specific dissipation rate or frequency scale ω. They are related to the more conventional turbulence variables, k and ε; the turbulent kinetic energy and its rate of dissipation through the following relations:

$$q = \sqrt{k}, \qquad \omega = \frac{\varepsilon}{k} \tag{12}$$

The q–ω turbulence model equations can be written in Cartesian tensor notation as

$$\begin{aligned}(\rho q)_{,t} + (\rho u_i q - k_q q_{,i})_{,i} &= H_q \\ (\rho\omega)_{,t} + (\rho u_i \omega - k_\omega \omega_{,i})_{,i} &= H_\omega\end{aligned} \tag{13}$$

where the diffusion constants for q and ω equations are

$$k_\omega = \mu_m + \frac{\mu_t}{\sigma_\omega}, \quad k_q = \mu_m + \frac{\mu_t}{\sigma_q} \tag{14}$$

The source terms in Equation (13) are given by

$$\begin{aligned}H_q &= C_{q1}\left(C_\mu f\,\frac{S}{\omega^2} - \frac{2D}{3\omega} - 1\right)\rho\omega q \\ H_\omega &= \left\{C_{\omega1}\left(C_\mu\frac{S}{\omega^2} - C_{\omega3}\,\frac{D}{\omega}\right) - C_{\omega2}\right\}\rho\omega^2\end{aligned} \tag{15}$$

where the strain rate invariant S, and the dilatation D, are defined by

$$\begin{aligned}S &= (u_{i,j} + u_{j,i})u_{i,j} - \tfrac{2}{3}D^2 \\ D &= u_{k,k}\end{aligned} \tag{16}$$

The eddy viscosity is obtained from the Prandtl–Kolmogorov relation

$$\mu_t = \frac{C_\mu f \rho q^2}{\omega} \tag{17}$$

The wall damping term, which accounts for the damping effect of solid walls, is given by

$$f = 1 - \mathrm{e}^{-0.022R}, \quad R = \frac{\rho q y}{\mu} \tag{18}$$

where y is the distance from the nearest solid wall. The model constants used in this paper are the same as given in Reference [9]

$$\begin{aligned}C_\mu = 0.09, \quad C_{q1} = 0.5, \quad C_{\omega1} = 0.5f + 0.055 \\ C_{\omega2} = 0.833, \quad C_{\omega3} = 2/3, \quad \sigma_q = 0.8, \quad \sigma_\omega = 2.0\end{aligned} \tag{19}$$

One of the advantages in using the q–ω model over other two-equation models is its numerical robustness. Unlike the k–ε model, the source terms is bounded near the solid wall. Also, it is known that the q–ω model is insensitive to the free-stream turbulent quantities and the initial condition. Due to the robustness of the q–ω model, all the computational results shown in this paper are obtained from uniform initial conditions. However, it is found to be often necessary to ramp up the *CFL* number over the period of a couple of hundreds iterations in order to suppress the non-linear instabilities at the beginning of the computations.

3. DISCRETIZATIONS

3.1. Spatial discretization

We will present the numerical methods and the stability analysis in a two-dimensional set-up for convenience. They are equally applicable to three-dimensional problems as well. The integral form of the Navier–Stokes equations in two-dimension can be written as

$$\frac{\partial}{\partial t}\int_{\Omega}\mathbf{Q}\,\mathrm{d}V+\oint_{\delta\Omega}\vec{\mathbf{F}}\cdot\hat{\mathbf{n}}\,\mathrm{d}S=\oint_{\delta\Omega}\vec{\mathbf{F}}_v\cdot\hat{\mathbf{n}}\,\mathrm{d}S+\int_{\Omega}\mathbf{S}_{q\omega}\,\mathrm{d}V \tag{20}$$

where the conservative vector $\mathbf{Q}$, the inviscid flux vector $\mathbf{F}$, the viscous flux vector $\mathbf{F}_v$, and the source term vector $\mathbf{S}_{q\omega}$, are defined by

$$\mathbf{Q}=\begin{bmatrix}\rho\\ \rho u\\ \rho v\\ e\\ \hline \rho q\\ \rho\omega\end{bmatrix},\quad \mathbf{F}=\vec{\mathbf{F}}\cdot\hat{\mathbf{n}}=\begin{bmatrix}\rho u_n\\ \rho u_n u+pn_x\\ \rho u_n v+pn_y\\ (e+p)u_n\\ \hline \rho u_n q\\ \rho u_n\omega\end{bmatrix},\quad \mathbf{F}_v=\vec{\mathbf{F}}_v\cdot\hat{\mathbf{n}}=\begin{bmatrix}0\\ n_x\tau_{xx}+n_y\tau_{xy}\\ n_x\tau_{yx}+n_y\tau_{yy}\\ \hat{\mathbf{n}}\cdot\vec{\mathbf{\Omega}}\\ \hline k_q\hat{\mathbf{n}}\cdot\nabla q\\ k_\omega\hat{\mathbf{n}}\cdot\nabla\omega\end{bmatrix},\quad \mathbf{S}_{q\omega}=\begin{bmatrix}0\\ 0\\ 0\\ 0\\ \hline H_q\\ H_\omega\end{bmatrix} \tag{21}$$

Here u_n is the normal velocity component to the boundary of the control volume, and the vector $\vec{\mathbf{\Omega}}$ is defined by

$$u_n=\hat{\mathbf{n}}\cdot\vec{\mathbf{v}}=n_x u+n_y v,\quad \vec{\mathbf{\Omega}}=\hat{\mathbf{n}}\cdot\vec{\vec{\mathbf{T}}}+k_T\nabla T \tag{22}$$

where $\vec{\vec{\mathbf{T}}}$ is the stress tensor.

If we integrate Equations (20) over a quadrilateral control volume, we have

$$V\frac{\partial\mathbf{Q}}{\partial t}+\sum\mathbf{F}\Delta S=\sum\mathbf{F}_v\Delta S+V\mathbf{S}_{q\omega} \tag{23}$$

where V and ΔS are the area of a quadrilateral cell, and length of the cell edges. In order to integrate Equation (23) numerically, the inviscid flux is replaced by Roe's numerical flux

$$\hat{\mathbf{F}}_{i+1/2}=\tfrac{1}{2}\{\mathbf{F}(\mathbf{Q}_R)+\mathbf{F}(\mathbf{Q}_L)-|\mathbf{K}|(\mathbf{Q}_R-\mathbf{Q}_L)\} \tag{24}$$

where $\mathbf{K}$ is the Jacobian matrix of the flux vector $\mathbf{F}$. MUSCL extrapolation for $\mathbf{Q}_L$ and $\mathbf{Q}_R$ is used for higher spatial accuracy. We use Van Albada's limiter to maintain total variation diminishing (TVD) property near sharp solution gradient region

$$\begin{aligned}Q_R|_{i-1/2}&=Q_i-\frac{s\sigma}{4}\{(1+s\kappa)\Delta_-+(1-s\kappa)\Delta_+\}\\ Q_L|_{i+1/2}&=Q_i+\frac{s\sigma}{4}\{(1-s\kappa)\Delta_-+(1+s\kappa)\Delta_+\}\end{aligned} \tag{25}$$

$$\Delta_+ = Q_{i+1} - Q_i, \qquad \Delta_- = Q_i - Q_{i-1}, \qquad s = \frac{2\Delta_+\Delta_- + \varepsilon}{\Delta_+^2 \Delta_-^2 + \varepsilon} \tag{26}$$

where ε is a small number to prevent singularity. All the computations presented in this paper were done with $\kappa = 1/3$, and $\varepsilon = 10^{-8}$. The dissipation term of Equation (24) can be written compactly as

$$|\mathbf{K}|(\mathbf{Q}_R - \mathbf{Q}_L) = \left(\delta\rho - \frac{\delta p}{c^2}\right)|\lambda_1'|\mathbf{P}_1 + \rho|\lambda_1'|\mathbf{P}_2 + \frac{\rho}{2c}\left(\frac{\delta p}{\rho c} + \delta u_n\right)|\lambda_3'|\mathbf{P}_3 + \frac{\rho}{2c}\left(\frac{\delta p}{\rho c} - \delta u_n\right)|\lambda_4'|\mathbf{P}_4 \tag{27}$$

where

$$\mathbf{P}_1 = \begin{bmatrix} 1 \\ u \\ v \\ \bar{Q} \\ \hline q \\ \omega \end{bmatrix}, \quad \mathbf{P}_2 = \begin{bmatrix} 0 \\ \delta u - n_x \delta u_n \\ \delta v - n_y \delta u_n \\ \delta\bar{Q} - u_n \delta u_n \\ \hline \delta q \\ \delta\omega \end{bmatrix}, \quad \mathbf{P}_3 = \begin{bmatrix} 1 \\ u + n_x c \\ v + n_y c \\ h + u_n c \\ \hline q \\ \omega \end{bmatrix}, \quad \mathbf{P}_4 = \begin{bmatrix} 1 \\ u - n_x c \\ v - n_y c \\ h - u_n c \\ \hline q \\ \omega \end{bmatrix} \tag{28}$$

and

$$\bar{Q} = \tfrac{1}{2}(u^2 + v^2) + C\zeta q^2, \qquad \delta\bar{Q} = u\delta u + v\delta v + 2C\zeta q \delta q \tag{29}$$

The eigenvalues, λ_i of the inviscid Jacobian matrix are given in Appendix A, and they are modified to enforce the entropy condition

$$|\lambda'| = \begin{cases} |\lambda| & \text{if } |\lambda| \geqslant \delta \\ \dfrac{1}{2}\left(\dfrac{|\lambda|^2}{\delta} + \delta\right) & \text{if } |\lambda| < \delta \end{cases} \tag{30}$$

We use $\delta = 0.25$ for all the computations in the paper.

The derivatives at half-node points needed for evaluating the viscous terms can be computed by applying the gradient theorem over an auxiliary cell depicted in Figure 1

$$\nabla\phi \approx \frac{1}{V}\oint_{\delta\Omega} \phi\hat{\mathbf{n}}\,\mathrm{d}S \tag{31}$$

This is equivalent to a familiar central difference formula, which uses 9-point compact stencil in two dimension and 27-point compact stencil in three dimension for the viscous terms. Because the auxiliary cell consists of the halves of neighbouring cells, the area and the normal vectors of the auxiliary cell can be computed directly from those of neighbouring computational cells. For instance, the area of the auxiliary cell is computed by averaging the

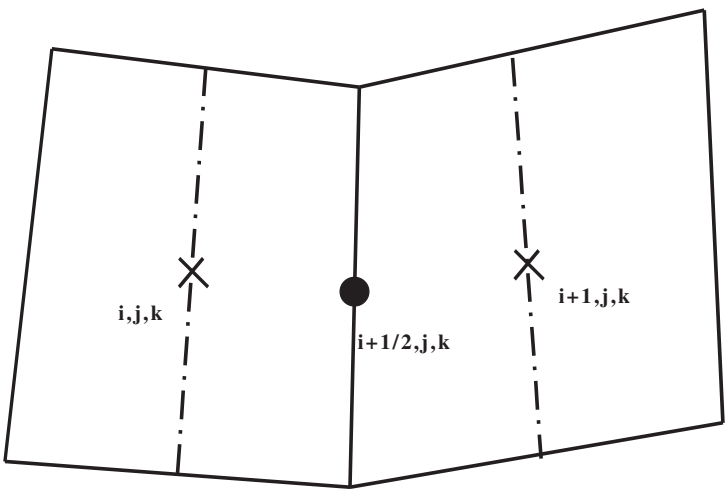

Figure 1. Auxiliary cell for derivatives at $i + 1/2$ point.

areas of the neighbouring two cells. Since in three-dimensional problems the volume of a computational cell is usually computed by summing the volumes of six tetrahedra which the computational cell is divided into, this approach gives big savings in CPU time. Also, we do not need nine variables per auxiliary cell needed for the storage of the normal vectors for three-dimensional problems.

3.2. Time stepping methods

We use the approximated factorization-alternate direction implicit (AF-ADI) method for the time stepping method. First, we consider the AF-ADI scheme for the strongly coupled method. The operator form of the AF-ADI scheme is found to be

$$\mathbf{L}_i \mathbf{P}^{-1} \mathbf{L}_j \Delta \mathbf{Q} = -\Delta t \mathbf{R} \tag{32}$$

where the factored operators and the residual vector are

$$\mathbf{L}_i = \left[\mathbf{P} + \frac{\Delta t}{V} \left\{ \left(\frac{\partial \tilde{\mathbf{F}}_{i+1/2}}{\partial \mathbf{Q}_{i+1}} + \frac{\partial \tilde{\mathbf{F}}_{i+1/2}}{\partial \mathbf{Q}_i} \right) \Delta S_{i+1/2} - \left(\frac{\partial \tilde{\mathbf{F}}_{i-1/2}}{\partial \mathbf{Q}_i} + \frac{\partial \tilde{\mathbf{F}}_{i-1/2}}{\partial \mathbf{Q}_{i-1}} \right) \Delta S_{i-1/2} \right\} \right]$$

$$\mathbf{L}_j = \left[\mathbf{P} + \frac{\Delta t}{V} \left\{ \left(\frac{\partial \tilde{\mathbf{F}}_{j+1/2}}{\partial \mathbf{Q}_{j+1}} + \frac{\partial \tilde{\mathbf{F}}_{j+1/2}}{\partial \mathbf{Q}_j} \right) \Delta S_{j+1/2} - \left(\frac{\partial \tilde{\mathbf{F}}_{j-1/2}}{\partial \mathbf{Q}_j} + \frac{\partial \tilde{\mathbf{F}}_{j-1/2}}{\partial \mathbf{Q}_{j-1}} \right) \Delta S_{j-1/2} \right\} \right] \tag{33}$$

$$\mathbf{R} = \frac{1}{V} [(\tilde{\mathbf{F}} \Delta S)_{i+1/2} - (\tilde{\mathbf{F}} \Delta S)_{i-1/2} + (\tilde{\mathbf{F}} \Delta S)_{j+1/2} - (\tilde{\mathbf{F}} \Delta S)_{j-1/2}] - \mathbf{S}_{q\omega} \tag{34}$$

Here, we have used the following symbols to avoid a lengthy mathematical formula:

$$\tilde{\mathbf{F}} = \hat{\mathbf{F}} - \mathbf{F}_v, \quad \mathbf{P} = \mathbf{I} - \Delta t \mathbf{D}, \quad \mathbf{D} = \frac{\partial \mathbf{S}_{q\omega}}{\partial \mathbf{Q}} \tag{35}$$

The derivatives of Roe's flux with respect to the solution vector are approximated by the following equations in order to reduce computational efforts:

$$\begin{aligned} \frac{\partial \hat{\mathbf{F}}_{i+1/2}}{\partial \mathbf{Q}_{i+1}} &= \tfrac{1}{2}(\mathbf{K}_{i+1} - |\mathbf{K}|) \cong \tfrac{1}{2}(\mathbf{K}_{i+1} - |\rho(\mathbf{K})|\mathbf{I}) \\ \frac{\partial \hat{\mathbf{F}}_{i+1/2}}{\partial \mathbf{Q}_{i}} &= \tfrac{1}{2}(\mathbf{K}_{i} + |\mathbf{K}|) \cong \tfrac{1}{2}(\mathbf{K}_{i} + |\rho(\mathbf{K})|\mathbf{I}) \end{aligned} \tag{36}$$

where $\rho(\mathbf{K})$ is the spectral radius of $\mathbf{K}$.

The first-order spatial discretization for the inviscid Jacobian terms was used for the implicit operators, which results in the system of block tri-diagonal matrices. These block tri-diagonal matrix systems can be easily solved with the Thomas algorithm. For better stability, only the turbulent destruction terms in the source terms are treated implicitly as done in Reference [3]. This makes the implicit operators diagonally dominant, resulting in more stable scheme. The Jacobian matrices of the flux vectors, the complete source terms and the turbulent destruction term in the source term are given in Appendix A.

According to Jongen and Marx [11], the strongly coupled method and the loosely coupled method may not be positive preserving due to the factorization error. However, the experiences indicate that the instability caused by the lack of the positivity usually occurs at the beginning of the computations. As stated earlier, the instability can be avoided if we increase the CFL number over a couple of hundred iterations at the beginning of the computations.

For the strongly coupled method, the Navier–Stokes equations and the q–ω turbulence model equations are solved simultaneously. Thus, 6×6 block tri-diagonal matrix system needs to be solved in order to update the solutions for two-dimensional problems. For the loosely coupled method, however, the Navier–Stokes equations are solved first with the turbulent viscosity fixed. Subsequently, the q–ω turbulence model equations are solved with the updated flow variables. Finally, the turbulent viscosity is updated with the Prandtl–Kolmogorov relation. Therefore, 4×4 block tri-diagonal matrix system and 2×2 block tri-diagonal matrix system have to be solved in order to update the solutions. Since it takes longer to solve a 6×6 block tri-diagonal matrix system than two smaller block tri-diagonal matrix systems, the CPU time of the strongly coupled method is usually larger than that of the loosely coupled method.

The first step of the loosely coupled method is given by

$$\mathbf{L}_i^{\mathrm{ns}} \mathbf{L}_j^{\mathrm{ns}} \Delta \mathbf{Q}^{\mathrm{ns}} = -\Delta t \mathbf{R}^{\mathrm{ns}} \tag{37}$$

where the solution vector is $\mathbf{Q}^{\mathrm{ns}} = [\rho \ \ \rho u \ \ \rho v \ \ e]^{\mathrm{T}}$, $\mathbf{R}^{\mathrm{ns}}$ is the residual vector of the Navier–Stokes equations that consists of the first four elements of Equation (34), and the implicit operators, $\mathbf{L}_i^{\mathrm{ns}}$ and $\mathbf{L}_j^{\mathrm{ns}}$ are similar to those in Equation (33). The solution vector of the q–ω turbulence model equations $\mathbf{Q}^{q\omega} = [\rho q \ \ \rho\omega]^{\mathrm{T}}$ can be updated by evaluating the following

equations:

$$\mathbf{L}_i^{q\omega}\mathbf{P}_{q\omega}^{-1}\mathbf{L}_j^{q\omega}\Delta\mathbf{Q}^{q\omega} = -\Delta t\mathbf{R}^{q\omega} \tag{38}$$

where $\mathbf{R}^{q\omega}$ is evaluated with the updated $\mathbf{Q}^{\mathrm{ns}}$.

Even though both coupling methods when used with the AF-ADI method are unconditionally stable according to the linear von Neumann stability analysis, the nonlinear stability behaviour of the scheme as well as the factorization error associated with the AF-ADI method could limit the time step in real applications. The time step is estimated from the following formula:

$$\Delta t = \frac{\Delta t_i \Delta t_j}{\Delta t_i + \Delta t_j} \tag{39}$$

where

$$\frac{1}{\Delta t_i} = \frac{|\rho(\mathbf{K})|}{CFL}\frac{\Delta S}{V} + \frac{\rho(\mathbf{K}_v)}{VN}\left(\frac{\Delta S}{V}\right)^2 \tag{40}$$

The expression for Δt_j assumes the similar form. Here, *CFL* is the Courant–Friedrichs–Lewy number and *VN* is the von Neuman number. The local time stepping strategy is adopted for better convergence. The spectral radii of the inviscid and viscous Jacobian matrices are given in Appendix A. Since *VN* is relevant for diffusion problems, it is often possible to use a large value of *VN* for external flows where convection is dominant.

3.3. Boundary conditions

The explicit treatment of the boundary conditions is widely used because of its simplicity. In the present study, the boundary conditions are applied explicitly and comparisons of the convergence characteristics of the two coupling methods are made. We note, however, it may change the stability of the present implicit numerical method. Two types of wall boundary conditions for the turbulence model equations are used. If the turbulence model equations are integrated to the wall, we use the non-slip boundary conditions for the mean flow. The turbulent velocity scale is set to zero at the wall, while the normal gradient of the specific dissipation rate is set to zero at the wall

$$q = 0, \qquad \frac{\partial\omega}{\partial n} = 0 \tag{41}$$

If the wall function is used, the slip wall boundary condition is used. The amount of slip is determined to give the same value of wall shear stress computed from the wall function as described in References [12, 13]. The turbulent velocity scale and the specific dissipation rate are evaluated with the following equations:

$$q = \frac{u_\tau}{C_\mu^{1/4}}, \qquad \omega = \frac{\sqrt{C_\mu}u_\tau}{k_v y} \tag{42}$$

where u_τ is the friction velocity which is determined from the wall function, and k_v is the von Karman constant of 0.41. We use the standard boundary conditions for the inflow and exit boundaries, which can be found in References [5, 10].

4. VON NEUMANN STABILITY ANALYSIS

4.1. Strongly coupled method

We will consider the stability of the strongly coupled method and the loosely coupled method applied to two-dimensional problems with the AF-ADI scheme. This procedure can be applied to three-dimensional problems in the same manner. The linearized system of the Navier–Stokes equations and the q–ω turbulence model equations in the Cartesian coordinates, can be written as

$$\frac{\partial \mathbf{Q}}{\partial t} + \mathbf{A}\frac{\partial \mathbf{Q}}{\partial x} + \mathbf{B}\frac{\partial \mathbf{Q}}{\partial y} = \mathbf{C}_{xx}\frac{\partial^2 \mathbf{Q}}{\partial x^2} + \mathbf{C}_{yy}\frac{\partial^2 \mathbf{Q}}{\partial y^2} + \mathbf{C}_{xy}\frac{\partial^2 \mathbf{Q}}{\partial x \partial y} + \mathbf{D}\mathbf{Q} \tag{43}$$

The inviscid Jacobian matrices appeared in Equation (43) are given by

$$\mathbf{A} = \left[\begin{array}{c|c} \mathbf{A}^{\mathrm{ns}} & \mathbf{A}^{u} \\ \hline \mathbf{A}^{d} & \mathbf{A}^{q\omega} \end{array}\right]$$

$$= \left[\begin{array}{cccc|cc} 0 & 1 & 0 & 0 & 0 & 0 \\ (\gamma-1)\bar{Q}-u^2 & (3-\gamma)u & (1-\gamma)v & \gamma-1 & -2C\zeta(\gamma-1)q & 0 \\ -uv & v & u & 0 & 0 & 0 \\ \{(\gamma-1)\bar{Q}-h\}u & h-(\gamma-1)u^2 & (1-\gamma)uv & \gamma u & -2C\zeta(\gamma-1)uq & 0 \\ \hline -uq & q & 0 & 0 & u & 0 \\ -u\omega & \omega & 0 & 0 & 0 & u \end{array}\right] \tag{44}$$

$$\mathbf{B} = \left[\begin{array}{c|c} \mathbf{B}^{\mathrm{ns}} & \mathbf{B}^{u} \\ \hline \mathbf{B}^{d} & \mathbf{B}^{q\omega} \end{array}\right]$$

$$= \left[\begin{array}{cccc|cc} 0 & 0 & 1 & 0 & 0 & 0 \\ -uv & v & u & 0 & 0 & 0 \\ (\gamma-1)\bar{Q}-v^2 & (1-\gamma)u & (3-\gamma)v & \gamma-1 & -2C\zeta(\gamma-1)q & 0 \\ \{(\gamma-1)\bar{Q}-h\}v & (1-\gamma)uv & h-(\gamma-1)v^2 & \gamma v & -2C\zeta(\gamma-1)vq & 0 \\ \hline -vq & 0 & q & 0 & v & 0 \\ -v\omega & 0 & \omega & 0 & 0 & v \end{array}\right] \tag{45}$$

while the viscous Jacobian matrices are given by

$$\mathbf{C}_{xx} = \left[\begin{array}{c|c} \mathbf{C}_{xx}^{\mathrm{ns}} & \mathbf{C}_{xx}^{u} \\ \hline \mathbf{C}_{xx}^{d} & \mathbf{C}_{xx}^{q\omega} \end{array}\right]$$

$$= \frac{1}{\rho}\left[\begin{array}{cccc|cc} 0 & 0 & 0 & 0 & 0 & 0 \\ -\dfrac{4\mu_T}{3}u & \dfrac{4\mu_T}{3} & 0 & 0 & 0 & 0 \\ -\mu_T v & 0 & \mu_T & 0 & 0 & 0 \\ k_1 & \left(\dfrac{4}{3}\mu_T - k_0 k_T\right)u & (\mu_T - k_0 k_T)v & k_0 k_T & -2k_0 k_T \zeta q & 0 \\ \hline -k_q q & 0 & 0 & 0 & k_q & 0 \\ -k_\omega \omega & 0 & 0 & 0 & 0 & k_\omega \end{array}\right] \tag{46}$$

$$\mathbf{C}_{yy} = \left[\begin{array}{c|c} \mathbf{C}_{yy}^{\mathrm{ns}} & \mathbf{C}_{yy}^{u} \\ \hline \mathbf{C}_{yy}^{d} & \mathbf{C}_{yy}^{q\omega} \end{array}\right]$$

$$= \frac{1}{\rho}\left[\begin{array}{cccc|cc} 0 & 0 & 0 & 0 & 0 & 0 \\ -\mu_T u & \mu_T & 0 & 0 & 0 & 0 \\ -\dfrac{4\mu_T}{3}v & 0 & \dfrac{4\mu_T}{3} & 0 & 0 & 0 \\ k_1 & (\mu_T - k_0 k_T)u & \left(\dfrac{4}{3}\mu_T - k_0 k_T\right)v & k_0 k_T & -2k_0 k_T \zeta q & 0 \\ \hline -k_q q & 0 & 0 & 0 & k_q & 0 \\ -k_\omega \omega & 0 & 0 & 0 & 0 & k_\omega \end{array}\right] \tag{47}$$

The Jacobian matrix for cross derivative term is found to be

$$\mathbf{C}_{xy} = \left[\begin{array}{c|c} \mathbf{C}_{xy}^{\mathrm{ns}} & \mathbf{C}_{xy}^{u} \\ \hline \mathbf{0} & \mathbf{0} \end{array}\right]$$

$$= \frac{1}{\rho}\left[\begin{array}{cccc|cc} 0 & 0 & 0 & 0 & 0 & 0 \\ -\dfrac{\mu_T}{3}v & 0 & \dfrac{\mu_T}{3} & 0 & 0 & 0 \\ -\dfrac{\mu_T}{3}u & \dfrac{\mu_T}{3} & 0 & 0 & 0 & 0 \\ k_3 & \dfrac{\mu_T}{3}u - 2k_0 k_T v & \dfrac{\mu_T}{3}v - 2k_0 k_T u & 2k_0 k_T & -2k_0 k_T \zeta q & 0 \\ \hline 0 & 0 & 0 & 0 & 0 & 0 \\ 0 & 0 & 0 & 0 & 0 & 0 \end{array}\right] \tag{48}$$

where the constants appeared in the above equations are

$$k_0 = \gamma - 1, \quad k_4 = 2q^2 + u^2 + v^2 - \frac{e}{\rho}, \quad k_1 = k_0 k_4 k_T - \mu_T(\tfrac{4}{3}u^2 + v^2)$$
$$k_2 = k_0 k_4 k_T - \mu_T(u^2 + \tfrac{4}{3}v^2), \quad k_3 = 2k_0 k_4 k_T - \tfrac{2}{3}\mu_T uv \tag{49}$$

The final discretized form of the linearized Navier–Stokes equations and the q–ω turbulence model equations for the strongly coupled method can be written as

$$\mathbf{L}_i \mathbf{P}^{-1} \mathbf{L}_j \Delta\mathbf{Q} = -\Delta t \mathbf{R} \tag{50}$$

where the implicit operators are

$$\mathbf{L}_i = \left\{ \mathbf{P} + \Delta t \left(\mathbf{A}\frac{\partial}{\partial x} - \mathbf{C}_{xx}\frac{\partial^2}{\partial x^2} \right) \right\}, \qquad \mathbf{L}_j = \left\{ \mathbf{P} + \Delta t \left(\mathbf{B}\frac{\partial}{\partial y} - \mathbf{C}_{yy}\frac{\partial^2}{\partial y^2} \right) \right\} \tag{51}$$

and the residual vector is

$$\mathbf{R} = \begin{bmatrix} \mathbf{R}^{\mathrm{ns}} \\ \mathbf{R}^{q\omega} \end{bmatrix} = \mathbf{A}\frac{\partial \mathbf{Q}}{\partial x} + \mathbf{B}\frac{\partial \mathbf{Q}}{\partial y} - \mathbf{C}_{xx}\frac{\partial^2 \mathbf{Q}}{\partial x^2} - \mathbf{C}_{yy}\frac{\partial^2 \mathbf{Q}}{\partial y^2} - \mathbf{C}_{xy}\frac{\partial^2 \mathbf{Q}}{\partial x \partial y} - \mathbf{D}\mathbf{Q} \tag{52}$$

By substituting $\mathbf{Q} = \bar{\mathbf{Q}}(t)\mathrm{e}^{\hat{\mathrm{i}}(i\theta_x + j\theta_y)}$ into Equation (50), we can obtain the amplification matrix of the discretized equations with the definition of the amplification matrix, $\bar{\mathbf{Q}}(t+\Delta t) = \mathbf{G}\bar{\mathbf{Q}}(t)$. Here, θ_x, θ_y are related with the wavenumbers through $\theta_x = k_x \Delta x$, $\theta_y = k_y \Delta y$. Also, i, j are the grid index in x and y coordinates, respectively and $\hat{\mathrm{i}} = \sqrt{-1}$. The amplification factor of the AF-ADI scheme with the strongly coupled method is found to be

$$g = \rho(\mathbf{G}) = \rho(\mathbf{K}_1^{-1}\mathbf{K}_2) \tag{53}$$

where

$$\mathbf{K}_1 = \mathbf{P} + \mathbf{W} + \Delta t \left[\hat{\mathrm{i}} \left(\frac{\mathbf{A}}{\Delta x} s_x + \frac{\mathbf{B}}{\Delta y} s_y \right) + \left(\frac{|\mathbf{A}|}{\Delta x} + \frac{2\mathbf{C}_{xx}}{\Delta x^2} \right) C_x + \left(\frac{|\mathbf{B}|}{\Delta y} + \frac{2\mathbf{C}_{yy}}{\Delta y^2} \right) C_y \right]$$
$$\mathbf{K}_2 = \mathbf{P} + \mathbf{W} + \Delta t \left[\hat{\mathrm{i}} \left(\frac{\mathbf{A}}{\Delta x} f_x + \frac{\mathbf{B}}{\Delta y} f_y \right) + \frac{|\mathbf{A}|}{\Delta x} g_x + \frac{|\mathbf{B}|}{\Delta y} g_y - \frac{\mathbf{C}_{xy}}{\Delta x \Delta y} s_x s_y \right] \tag{54}$$

Here the factorization error is given by

$$\mathbf{W} = \Delta t^2 \left\{ \frac{\hat{\mathrm{i}}\mathbf{A}}{\Delta x} s_x + \left(\frac{|\mathbf{A}|}{\Delta x} + \frac{2\mathbf{C}_{xx}}{\Delta x^2} \right) C_x \right\} \left\{ \frac{\hat{\mathrm{i}}\mathbf{B}}{\Delta y} s_y + \left(\frac{|\mathbf{B}|}{\Delta y} + \frac{2\mathbf{C}_{yy}}{\Delta y^2} \right) C_y \right\} \tag{55}$$

The coefficients in Equations (54) and (55) are

$$f_x = \sigma \frac{1-\kappa}{4}(s_{2x} - 2s_x), \quad g_x = \sigma \left\{ \frac{1-\kappa}{4}(C_{2x} - 2C_x) + \frac{1+\kappa}{2} C_x \right\}$$
$$s_x = \sin\theta_x, \quad C_x = 1 - \cos\theta_x, \quad s_{2x} = \sin 2\theta_x, \quad C_{2x} = 1 - \cos 2\theta_x \tag{56}$$

and f_y, g_y, s_x, s_{2x}, C_x, and C_{2x} take the similar form.

4.2. Loosely coupled method

We follow Lee and Dulikravich's approach to study the stability of the loosely coupled method with the AF-ADI scheme. First, we define the composite solution vector, $\mathbf{Q}_c$ by

$$\mathbf{Q}_c = \begin{bmatrix} \mathbf{Q}^{\mathrm{ns}} \\ \hline \mathbf{Q}^{q\omega} \end{bmatrix} \tag{57}$$

The first four components of the composite solution vector are from the Navier–Stokes equations while the last two components are from the q–ω turbulence model equations. Then the two-step method can be written as

$$\begin{aligned} \mathbf{L}_i^{(1)}\mathbf{L}_j^{(1)}\Delta\mathbf{Q}_c^{(1)} &= -\Delta t\mathbf{R}^{(1)} \\ \mathbf{L}_i^{(2)}\mathbf{P}^{-1}\mathbf{L}_j^{(2)}\Delta\mathbf{Q}_c^{(2)} &= -\Delta t\mathbf{R}^{(2)} \end{aligned} \tag{58}$$

where the corrections are defined by

$$\Delta\mathbf{Q}_c^{(1)} = \mathbf{Q}_c^* - \mathbf{Q}_c^n, \qquad \Delta\mathbf{Q}_c^{(2)} = \mathbf{Q}_c^{n+1} - \mathbf{Q}_c^* \tag{59}$$

Here $\mathbf{Q}_c^*$ is the intermediate solution vector. The implicit operators of the first step are given by

$$\mathbf{L}_i^{(1)} = \left\{\mathbf{I} + \Delta t\left(\mathbf{A}^{(1)}\frac{\partial}{\partial x} - \mathbf{C}_{xx}^{(1)}\frac{\partial^2}{\partial x^2}\right)\right\}, \qquad \mathbf{L}_j^{(1)} = \left\{\mathbf{I} + \Delta t\left(\mathbf{B}^{(1)}\frac{\partial}{\partial y} - \mathbf{C}_{yy}^{(1)}\frac{\partial^2}{\partial y^2}\right)\right\} \tag{60}$$

where the Jacobian matrices in the implicit operators are

$$\begin{aligned} \mathbf{A}^{(1)} &= \left[\begin{array}{c|c} \mathbf{A}^{\mathrm{ns}} & \mathbf{0} \\ \hline \mathbf{0} & \mathbf{I} \end{array}\right], \qquad \mathbf{B}^{(1)} = \left[\begin{array}{c|c} \mathbf{B}^{\mathrm{ns}} & \mathbf{0} \\ \hline \mathbf{0} & \mathbf{I} \end{array}\right] \\ \mathbf{C}_{xx}^{(1)} &= \left[\begin{array}{c|c} \mathbf{C}_{xx}^{\mathrm{ns}} & \mathbf{0} \\ \hline \mathbf{0} & \mathbf{I} \end{array}\right], \quad \mathbf{C}_{yy}^{(1)} = \left[\begin{array}{c|c} \mathbf{C}_{yy}^{\mathrm{ns}} & \mathbf{0} \\ \hline \mathbf{0} & \mathbf{I} \end{array}\right], \quad \mathbf{R}^{(1)} = \left[\begin{array}{c} \mathbf{R}^{\mathrm{ns}} \\ \hline \mathbf{0} \end{array}\right] \end{aligned} \tag{61}$$

The implicit operators for the second step take the similar form as those of the first step. The difference, however, comes from the source term. The implicit operators are found to be

$$\begin{aligned} \mathbf{L}_i^{(2)} &= \left\{\mathbf{P} + \Delta t\left(\mathbf{A}^{(2)}\frac{\partial}{\partial x} - \mathbf{C}_{xx}^{(2)}\frac{\partial^2}{\partial x^2}\right)\right\}, \qquad \mathbf{L}_j^{(2)} = \left\{\mathbf{P} + \Delta t\left(\mathbf{B}^{(2)}\frac{\partial}{\partial y} - \mathbf{C}_{yy}^{(2)}\frac{\partial^2}{\partial y^2}\right)\right\} \\ \mathbf{P} &= \mathbf{I} - \Delta t\left[\begin{array}{c|c} \mathbf{0} & \mathbf{0} \\ \hline \mathbf{0} & \mathbf{D}^{q\omega} \end{array}\right] \end{aligned} \tag{62}$$

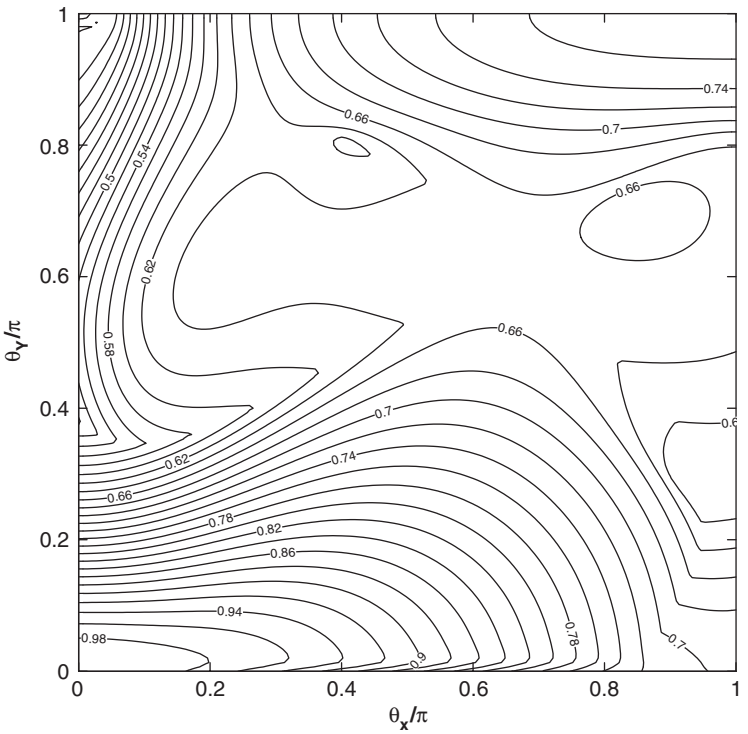

Figure 2. Amplification factor contours of the strongly coupled method for $M = 0.435$, $Re = 1 \times 10^7$, $v/u = 0$, $\Delta x = 0.02$, $\Delta y = 0.001$, $q = 0.1$, $\omega = 20$, $\zeta = 1$.

where the Jacobian matrices are

$$\mathbf{A}^{(2)} = \left[\begin{array}{c|c} \mathbf{I} & \mathbf{0} \\ \hline \mathbf{0} & \mathbf{A}^{q\omega} \end{array}\right], \qquad \mathbf{B}^{(2)} = \left[\begin{array}{c|c} \mathbf{I} & \mathbf{0} \\ \hline \mathbf{0} & \mathbf{B}^{q\omega} \end{array}\right]$$

$$\mathbf{C}_{xx}^{(2)} = \left[\begin{array}{c|c} \mathbf{I} & \mathbf{0} \\ \hline \mathbf{0} & \mathbf{C}_{xx}^{q\omega} \end{array}\right], \quad \mathbf{C}_{yy}^{(2)} = \left[\begin{array}{c|c} \mathbf{I} & \mathbf{0} \\ \hline \mathbf{0} & \mathbf{C}_{yy}^{q\omega} \end{array}\right], \quad \mathbf{R}^{(2)} = \left[\begin{array}{c} \mathbf{0} \\ \hline \mathbf{R}^{q\omega} \end{array}\right] \tag{63}$$

The Jacobian matrices $\mathbf{A}^{\mathrm{ns}}$, $\mathbf{B}^{\mathrm{ns}}$, etc. are the sub matrices found in Equations (44)–(48). The amplification factor of the AF-ADI scheme with the loosely coupled method can be calculated from

$$g = \rho(\mathbf{G}^{(1)}\mathbf{G}^{(2)}) \tag{64}$$

where $\mathbf{G}^{(1)}$ and $\mathbf{G}^{(2)}$ are the amplification matrices of the first and the second steps, which are found to be similar to Equations (53)–(55).

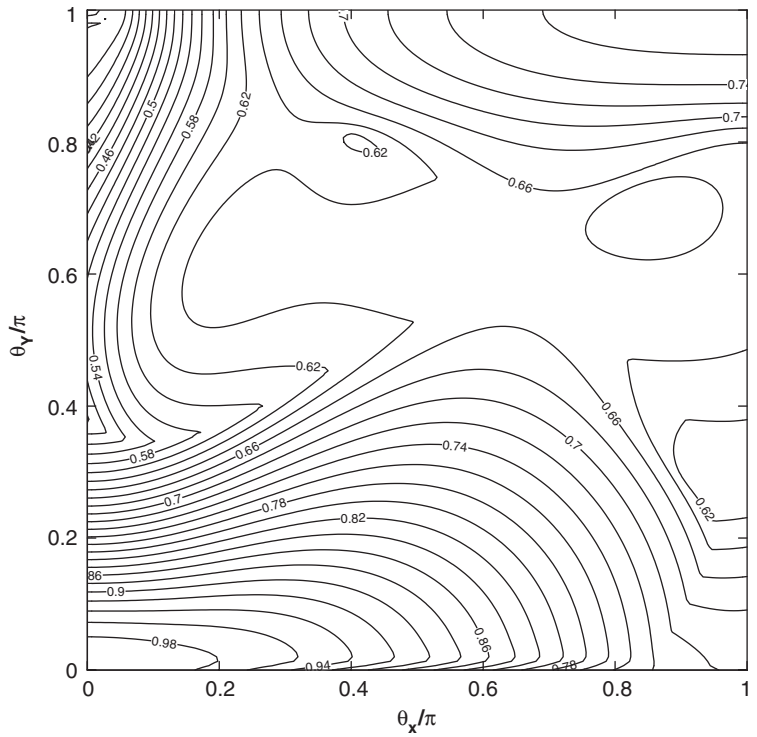

Figure 3. Amplification factor contours of the loosely coupled method for $M = 0.435$, $Re = 1 \times 10^7$, $v/u = 0$, $\Delta x = 0.02$, $\Delta y = 0.001$, $q = 0.1$, $\omega = 20$, $\zeta = 1$.

4.3. Stability analysis results

FORTRAN programs are developed to analyse the stability characteristics of the strongly coupled method and the loosely coupled method. Figures 2 and 3 show the stability results of both methods for the local Mach number and the Reynolds number of 0.435 and 1×10^7, respectively. The flow angle and the aspect ratio of the computational cell are 0 and 20. The values of the non-dimensionalized turbulent quantities, q and ω are chosen to be 0.1 and 20. These correspond to the turbulent viscosity that is 337.5 times as large as the molecular viscosity. These flow quantities are chosen from the computational results of the transonic flow around an RAE2822 airfoil, which is one of the computational examples. The ratio of the turbulent kinetic energy to that of free stream is slightly higher than 3.8%, which occurs at the edge of the boundary layer just aft of the shock where the turbulent kinetic energy is the highest. $CFL = 20$ and $VN = \infty$ are used to compute the time step. The turbulent kinetic energy contributions are included in these plots ($\zeta = 1$). Little difference can be noticed from the figures, indicating almost identical convergence behaviour of both methods. Figures 4 and 5 depict amplification factor contours for $\zeta = 0$. The other conditions are the same as those used in Figures 2 and 3. As can be seen in the figures, the stability characteristics of the strongly coupled method and the loosely coupled method are identical if the turbulent

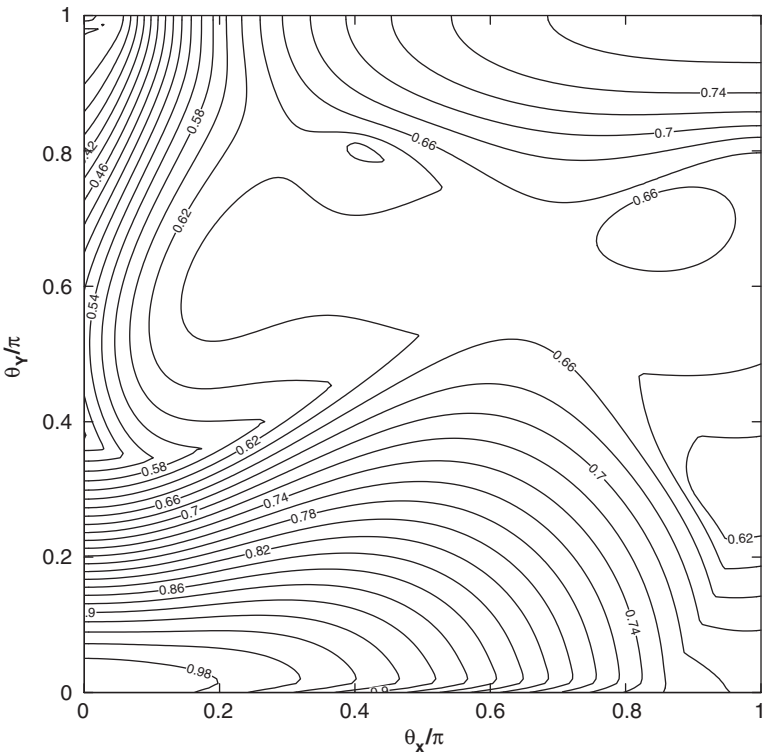

Figure 4. Amplification factor contours of the strongly coupled method for $M = 0.435$, $Re = 1 \times 10^7$, $v/u = 0$, $\Delta x = 0.02$, $\Delta y = 0.001$, $q = 0.1$, $\omega = 20$, $\zeta = 0$.

kinetic energy contributions to the momentum equations and the state equation are ignored. The identical stability characteristics can be deduced from the characteristics of the Jacobian matrices involved in the implicit operators. We will discuss it further in the next section. In Figures 6 and 7, the contours of constant amplification factors of both coupling methods with $\zeta = 1$ are presented when the kinetic energy is 25 times higher than the previous case. Even with such high values of kinetic energy, the figures show the stability characteristics of both methods are very similar.

4.4. Stability of both coupling methods with $\zeta = 0$

In this section, we will show that the stability characteristics of the strongly coupled method and the loosely coupled method are identical when $\zeta = 0$. First, we define a matrix of L-type as

$$\mathbf{L} = \left[\begin{array}{c|c} \mathbf{C} & \mathbf{0} \\ \hline \mathbf{D} & \mathbf{E} \end{array}\right] \tag{65}$$

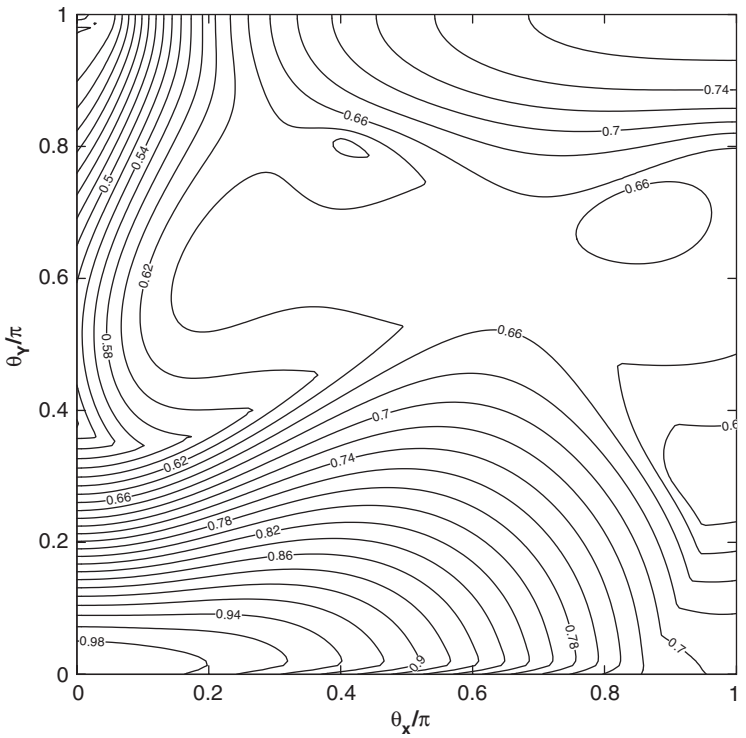

Figure 5. Amplification factor contours of the loosely coupled method for $M = 0.435$, $Re = 1 \times 10^7$, $v/u = 0$, $\Delta x = 0.02$, $\Delta y = 0.001$, $q = 0.1$, $\omega = 20$, $\zeta = 0$.

Then, this L-type matrix has the following properties:

1. Multiplication of two L-type matrices results in an L-type matrix, and the diagonal blocks of the resulting L-type matrices are the products of the diagonal blocks of the two matrices.

$$\left[\begin{array}{c|c} \mathbf{C} & \mathbf{0} \\ \hline \mathbf{D} & \mathbf{E} \end{array}\right] \left[\begin{array}{c|c} \mathbf{F} & \mathbf{0} \\ \hline \mathbf{G} & \mathbf{H} \end{array}\right] = \left[\begin{array}{c|c} \mathbf{CF} & \mathbf{0} \\ \hline \mathbf{DF} + \mathbf{EG} & \mathbf{EH} \end{array}\right] \tag{66}$$

2. Inverse of an L-type matrix is also an L-type matrix, and the diagonal blocks of the inverse matrix are the inverse of the diagonal blocks.

$$\left[\begin{array}{c|c} \mathbf{C} & \mathbf{0} \\ \hline \mathbf{D} & \mathbf{E} \end{array}\right]^{-1} = \left[\begin{array}{c|c} \mathbf{C}^{-1} & \mathbf{0} \\ \hline -\mathbf{E}^{-1}\mathbf{D}\mathbf{C}^{-1} & \mathbf{E}^{-1} \end{array}\right] \tag{67}$$

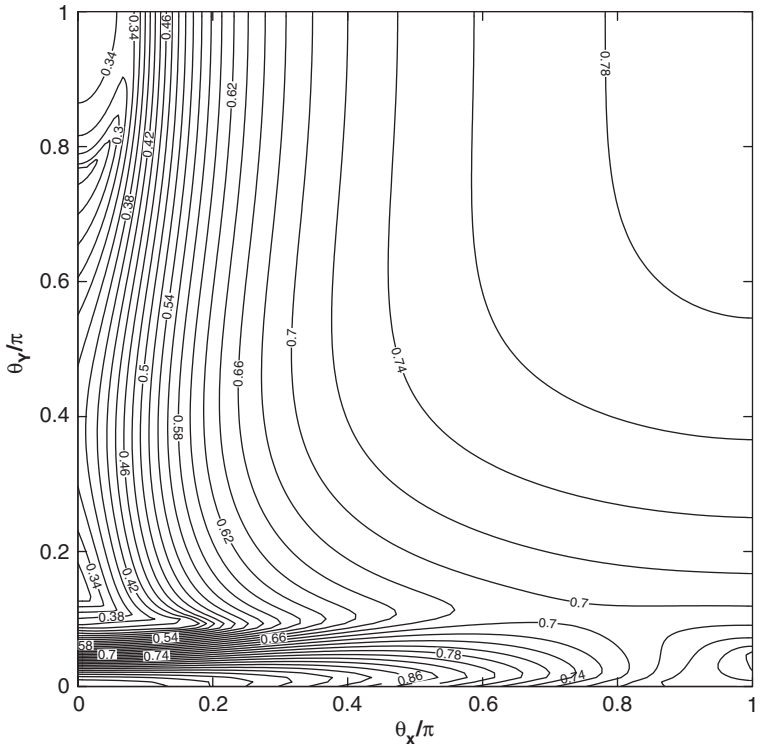

Figure 6. Amplification factor contours of the strongly coupled method for $M = 0.418$, $Re = 1 \times 10^7$, $v/u = 0$, $\Delta x = 0.02$, $\Delta y = 0.001$, $q = 0.5$, $\omega = 20$, $\zeta = 1$.

3. Eigenvalues of an L-type matrix consist of the eigenvalues of diagonal blocks of the matrix. The proof of the property can be found in Reference [14].

For $\zeta = 0$, we know that the matrices, $\mathbf{A}$, $\mathbf{B}$, $|\mathbf{A}|$, $|\mathbf{B}|$, $\mathbf{C}_{xx}$, $\mathbf{C}_{xy}$, $\mathbf{C}_{yy}$, and $\mathbf{P}$ for both methods are all L-type matrices. Therefore, the first diagonal block of $\mathbf{G}$ in Equation (53) is the same as the corresponding diagonal block of $\mathbf{G}^{(1)}$ in Equation (64), while the second diagonal block of $\mathbf{G}$ in Equation (53) is the same as the second diagonal block of $\mathbf{G}^{(2)}$ in Equation (64). We can conclude that from properties 1 and 2 the diagonal blocks of the amplification matrices of the strongly coupled method and the loosely coupled method are the same unless we change the sweep directions. Furthermore, they are L-type matrices. The amplification factors of both methods are the same due to property 3. The stability analysis of this section suggests that when the computational study on the chemical reaction or the real gas effects is considered, the species concentration equations and the continuity equation can be solved separately from the momentum and energy equations without loss of stability characteristics. However, the correct numerical method for the source terms has to be devised and applied in order to use the loosely coupled method efficiently.

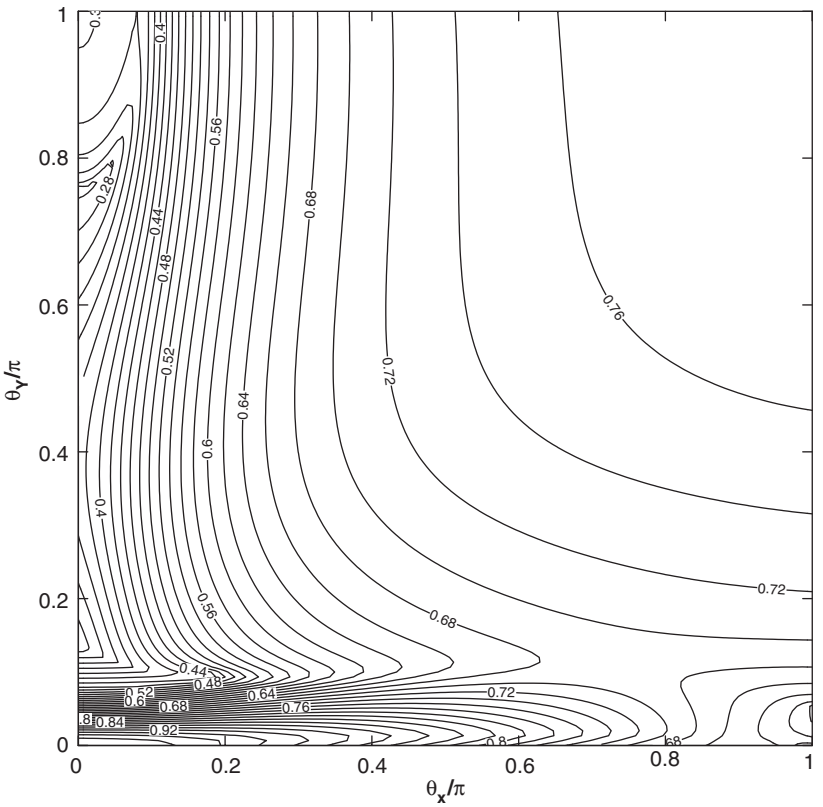

Figure 7. Amplification factor contours of the loosely coupled method for $M = 0.418$, $Re = 1 \times 10^7$, $v/u = 0$, $\Delta x = 0.02$, $\Delta y = 0.001$, $q = 0.5$, $\omega = 20$, $\zeta = 1$.

5. COMPUTATIONAL RESULTS

5.1. Transonic flow over RAE2882 airfoil

In order to confirm the results of stability analysis, transonic flows over the RAE2822 airfoil were computed with both coupling methods. The experimental data were reported by Cook *et al.* [15]. Computational results of the case 9 are presented here. The free-stream Mach number, the Reynolds number based on chord length, and the angle of attack are 0.73, 6.5×10^6 and 3.19°, respectively. A C-type grid of 297×65 is used and the number of cells on the airfoil surface is 200. Figure 8 shows the close-up view of the grid. The largest value of y^+ at the centre of the first cell off the wall is 32, which is well within the logarithmic region. We use the wall function to specify the boundary condition on the solid wall for this case. The surface pressure coefficients and the skin friction coefficients of the solvers are compared in Figures 9 and 10 with the experimental results, showing good agreement. While the coupling methods do not alter the results, the inclusion of the turbulent kinetic energy makes a slight change in the surface pressure and the skin friction coefficients distribution. All the

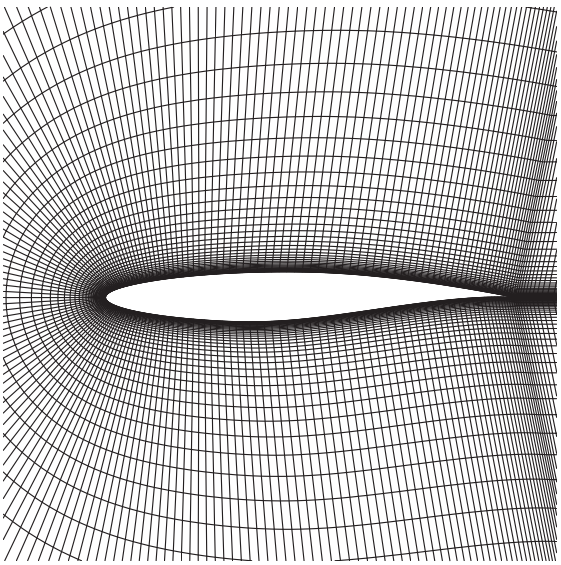

Figure 8. Close-up view of the grid used for the computation of flow around RAE 2822 airfoil.

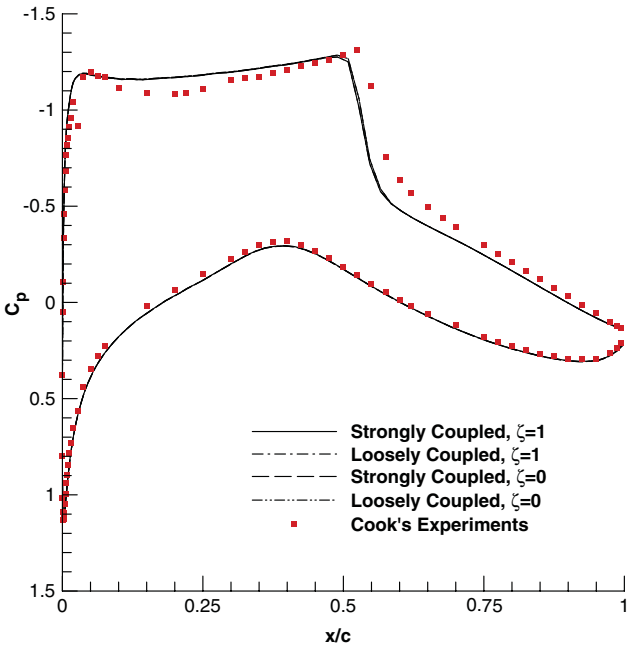

Figure 9. Comparison of the surface pressure coefficient distributions for transonic flow around RAE2822 airfoil at $M = 0.73$, $Re = 6.5 \times 10^6$, $\alpha = 3.19^\circ$ (wall function).

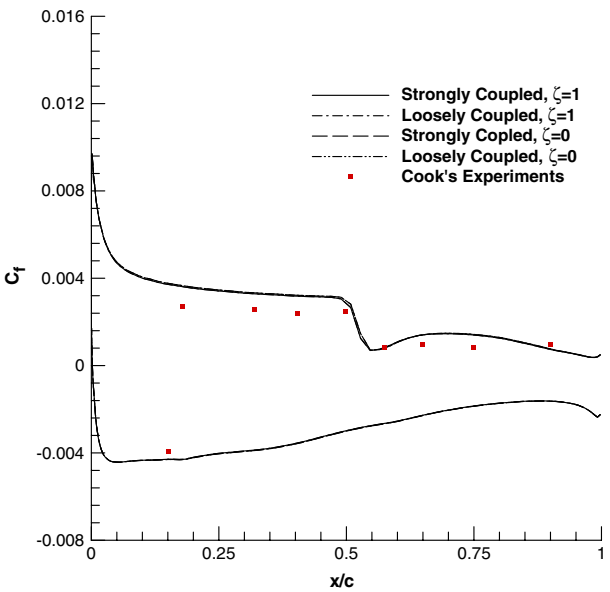

Figure 10. Comparison of the skin friction coefficient distributions for transonic flow around RAE2822 airfoil at $M = 0.73$, $Re = 6.5 \times 10^6$, $\alpha = 3.19^\circ$ (wall function).

results were obtained with $CFL = 20$ and $VN = \infty$. The convergence histories of both coupling methods are compared in Figure 11. In the figure, the RMS values of the residuals of the density and the turbulence quantities are presented. The overall convergence behaviours of both coupling methods are identical for either value of ζ. The slight difference shown in the convergence histories comes from the inclusion of the turbulent kinetic energy contribution, not from the difference of the coupling method used to solve the governing equations. As can be seen in the figure, the residuals of the Navier–Stokes equations as well as the turbulence model equations converge to machine zero within 5000 iterations for both coupling methods. The CPU time per cell per iteration for the strongly coupled method and the loosely coupled method are 35.6 and 20.7 μs, respectively. We used one CPU of a 12-node cluster (dual 2.4 GHz Intel Xeon processors) for this example. As stated earlier, the strongly coupled method takes longer to run than the loosely coupled method.

Figures 12 and 13 present the surface pressure coefficient and the skin friction coefficient of the RAE2822 airfoil with the same flow conditions as the previous case. In this example, we integrate the turbulence model equations to the wall. A C-type grid of 297×85 is used and the grid lines are more clustered toward the wall comparing with the grid used in the previous computation. The first cell centre points off the wall surface are located within 1.73 of y^+. The surface pressure coefficient and the skin friction coefficient are compared with the experimental data. The skin friction coefficient distribution indicates that the q–ω turbulence model can simulate the transition to turbulent flow. Figure 14 shows the comparison of the convergence behaviour of both coupling methods indicating a slower convergence than that of the previous results due to the highly clustered grid. However, after 6000 iterations the convergence exhibits a linear behaviour. The coupling methods do not change the convergence

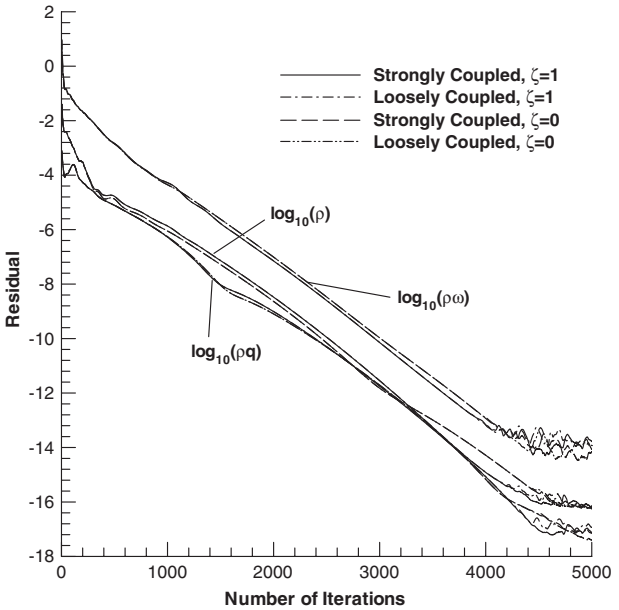

Figure 11. Comparison of the convergence histories of the strongly and the loosely coupled methods for transonic flow around RAE2822 airfoil at $M = 0.73$, $Re = 6.5 \times 10^6$, $\alpha = 3.19^\circ$ (wall function).

characteristics as in the previous case. The *CFL* number of 5 is used and the von Neumann number is not considered in determining the time step.

5.2. *Mesh size effects*

In order to see the mesh size effects on the convergence of both coupling strategies, three C-type grids of 231×56, 297×65, and 375×71 are used for the transonic flow over the RAE2822 airfoil. The wall function is used in this study. The performance of both coupling methods with $\zeta = 0$ and 1 is compared in Table I. The number of iterations given in the table is the value when the initial residual is reduced by 10 orders of magnitude. As can be seen in the table, the choice of the coupling methods does not change the convergence behaviour of the scheme. Also, the CPU time per cell per iteration is included in the table for comparison.

5.3. *Transonic flow over ONERA M-6 Wing*

As the second example, a transonic turbulent flow over the ONERA M-6 is computed with both the strongly coupled method and the loosely coupled method. The wall function approach is used to specify the solid wall boundary condition on the wing surface. The entire computational domain is subdivided into four blocks, and each block is discretized with $97 \times 33 \times 27$ grid. The wing surface is modeled with a surface patch of 129×34. The chord-wise pressure distributions at six span locations are compared with the experimental data by Schmitt and Charpin [16] in Figure 15. Since both coupling methods for either value of ζ give

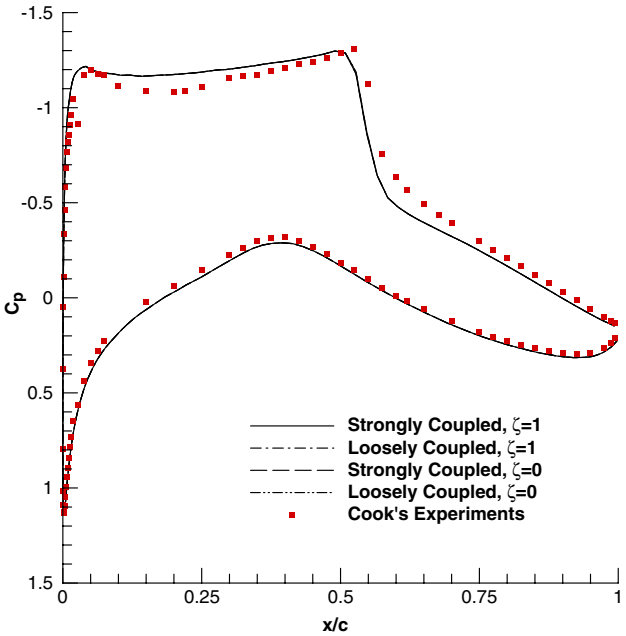

Figure 12. Comparison of the surface pressure coefficient distributions for transonic flow around RAE2822 airfoil at $M = 0.73$, $Re = 6.5 \times 10^6$, $\alpha = 3.19^\circ$ (without wall function).

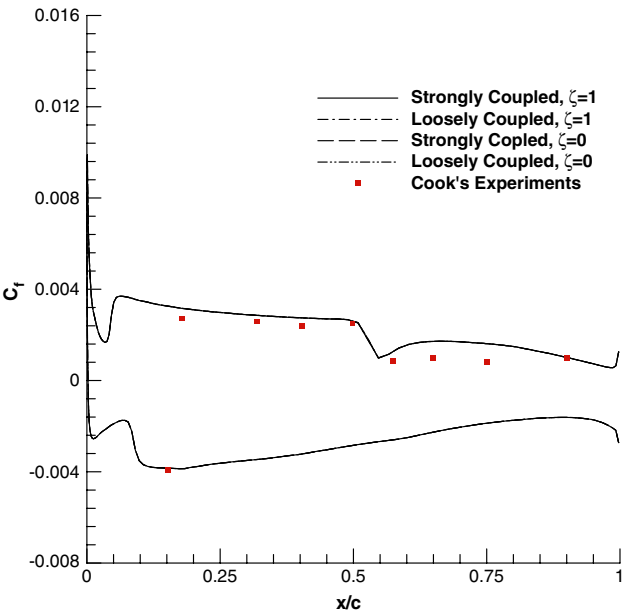

Figure 13. Comparison of the skin friction coefficient distributions for transonic flow around RAE2822 airfoil at $M = 0.73$, $Re = 6.5 \times 10^6$, $\alpha = 3.19^\circ$ (without wall function).

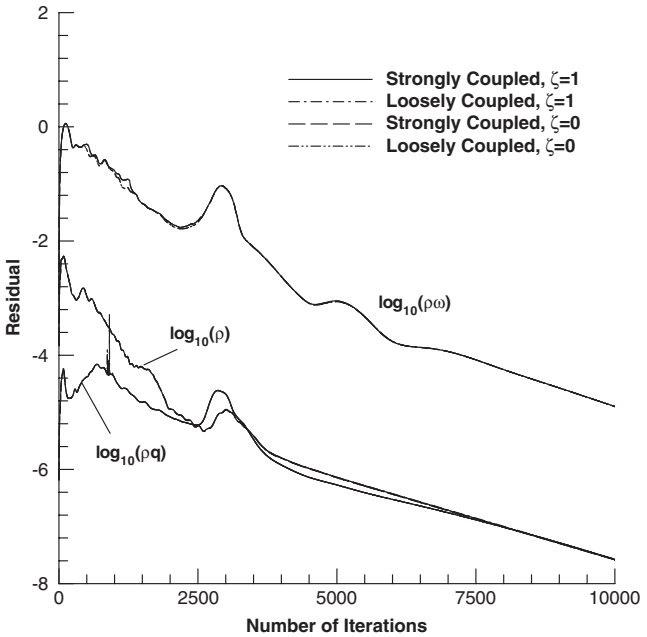

Figure 14. Comparison of the convergence histories of the strongly and the loosely coupled methods for transonic flow around RAE2822 airfoil at $M = 0.73$, $Re = 6.5 \times 10^6$, $\alpha = 3.19^\circ$ (without wall function).

Table I. Mesh size effects on the convergence of the coupling methods.

	Strongly coupled method			Loosely coupled method		
Grid size	$\zeta = 0$	$\zeta = 1$	CPU (μs)*	$\zeta = 0$	$\zeta = 1$	CPU (μs)*
231×56	3344	3433	33.1	3344	3436	19.6
297×65	3482	3470	35.6	3482	3472	20.7
375×71	3857	4068	37.2	3855	4072	20.7

*With one CPU of 12-node cluster (dual 2.4 GHz Intel Xeon processors).

indiscernible pressure coefficients, only the results from the strongly coupled method for $\zeta = 1$ are presented and compared with the experimental results. The figure indicates the computed surface pressure coefficients agree well with the experimental data. Both the computational results and the experimental results exhibit the formation of a lambda shock due to a merge of a leading edge shock and a trailing edge shock. In Figure 16, the convergence histories of the solvers are compared with each other. Again, no significant difference in convergence histories is noticed. All the computations for this case are done with $CFL = 5$, $VN = 5$. Almost 5 order of reduction in the residuals is obtained in 3000 iterations. The CPU time per cell per iteration for this example is 68.5 μs for the strongly coupled method and 45.6 μs for the loosely coupled method. We used four CPUs for this computation. The loosely coupled method runs about one and half times faster than the strongly coupled method.

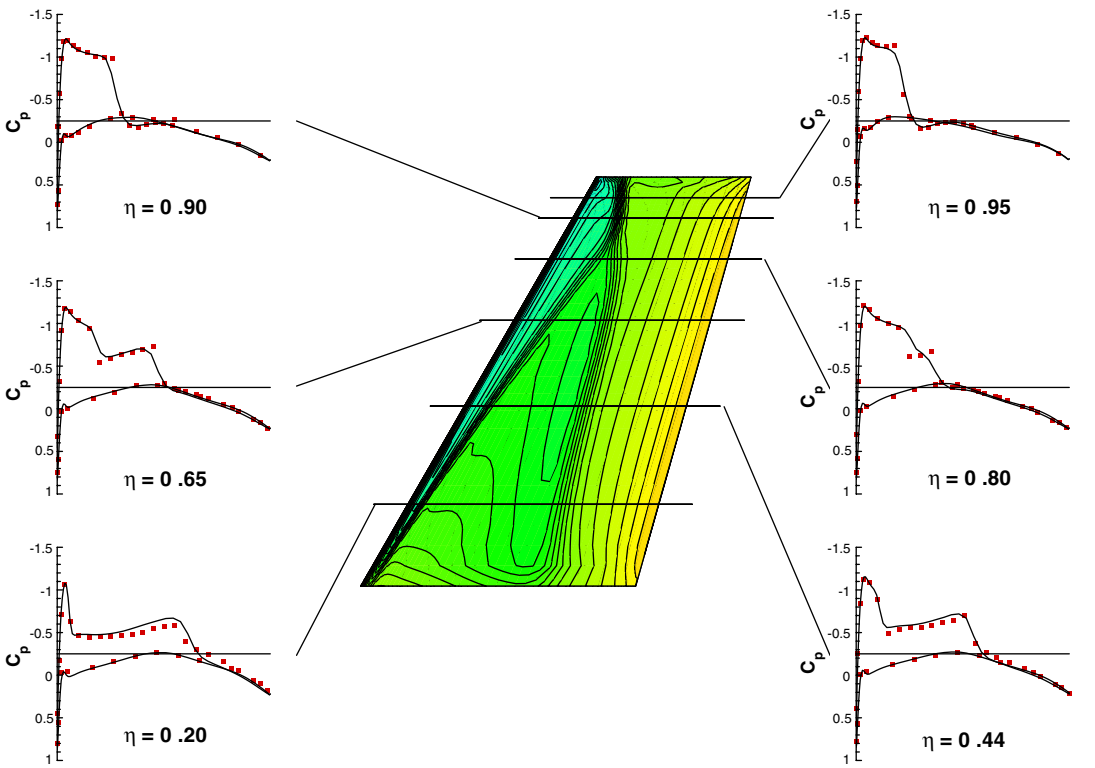

Figure 15. Surface pressure coefficient distributions of transonic flow around ONERA M-6 Wing at $M = 0.84$, $Re = 11.72 \times 10^6$, $\alpha = 3.06°$.

5.4. *Flow over RAE wing body*

Figure 17 depicts the surface grid of the RAE wing body for the next computational example. Treadgold *et al.* [17] measured the surface pressure distributions not only on the wing but on the body using an 8 ft $\times$ 6 ft transonic wind tunnel. The computational domain is discretized with a six block grid system. The sizes of each blocks are $71 \times 41 \times 55$. In this example, we integrated the turbulence equations to the wall to see the grid clustering effects on the convergence for three-dimensional problems. In Figure 18, the pressure coefficient distributions on the fuselage along the constant circumferential angles of ± 15, ± 30, ± 45 and $\pm 75°$ are compared with the experimental data. The circumferential angle is measured from the wing surface and the positive angles indicate the upper fuselage. Slight differences in the surface pressure coefficients at $\phi = \pm 75°$ can be seen. Otherwise, the computed results indicate good agreement with the experimental data. The surface pressure coefficient distributions at seven span locations on the wing surface are compared in Figure 19, showing excellent agreement with the experimental results. Since the results from the two solvers are identical, we presented the results from the strongly coupled method with $\zeta = 1$ only. In Figure 20, the convergence

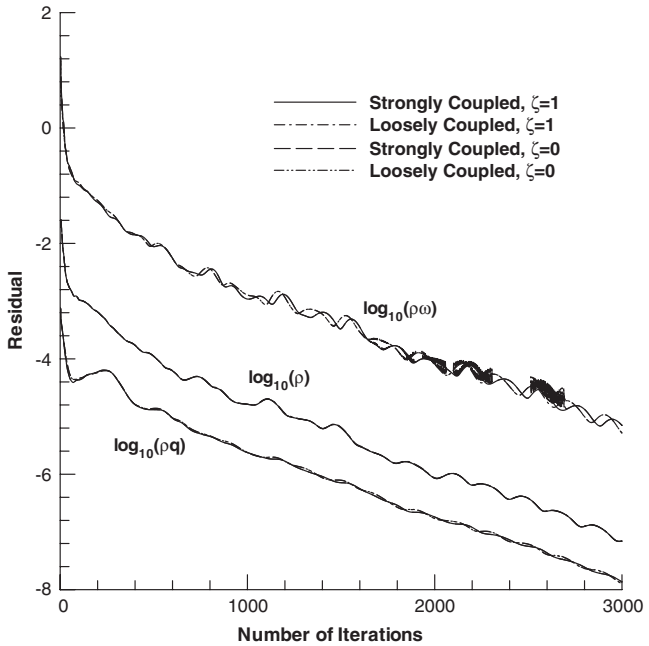

Figure 16. Comparison of the convergence histories of the strongly and the loosely coupled methods for transonic flow over ONERA M-6 Wing at $M = 0.84$, $Re = 11.72 \times 10^6$, $\alpha = 3.06^\circ$.

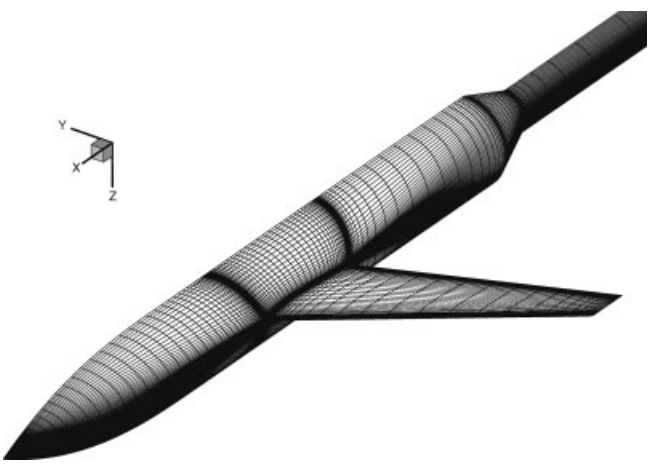

Figure 17. A surface grid of RAE wing body problem.

histories of both coupling methods are presented. As in the previous cases, the convergence characteristics of both coupling methods are almost identical for either value of ζ, showing that the coupling methods do not change the convergence behaviour. The *CFL* number and

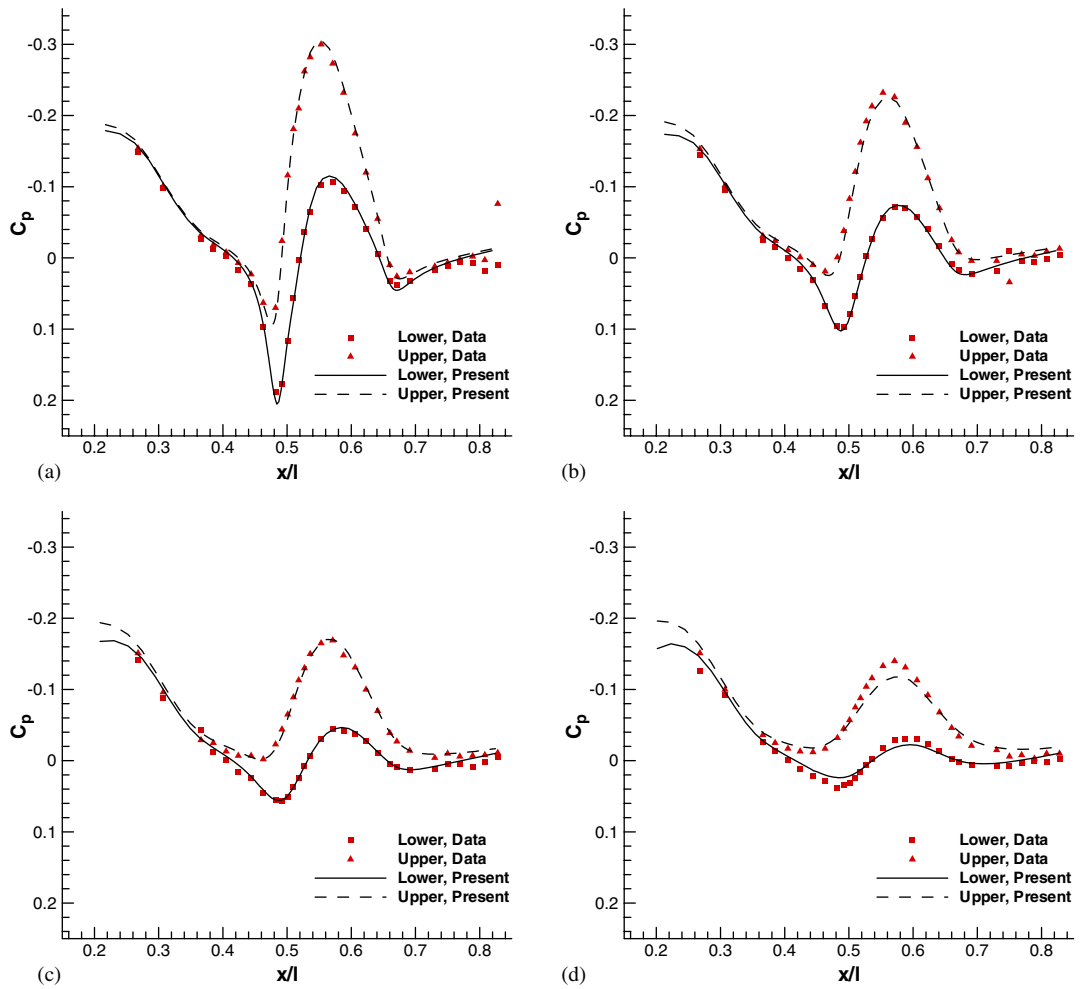

Figure 18. Surface pressure coefficient distributions on the body of RAE wing body at $M = 0.8$, $Re = 1.0 \times 10^6$, $\alpha = 2°$: (a) $\phi = \pm 15°$; (b) $\phi = \pm 30°$; (c) $\phi = \pm 45°$; and (d) $\phi = \pm 75°$.

VN used in this computation are 5 and 0.5, respectively. The CPU time per cell per iteration with six CPUs is 85.3 μs for the strongly coupled method and 49.4 μs for the loosely coupled method.

6. CONCLUDING REMARKS

The loosely coupled method and the strongly coupled method for the Navier–Stokes equations and the q–ω turbulence model equations are developed and applied to a number of computational examples including two- and three-dimensional problems. The methods use the AF-ADI

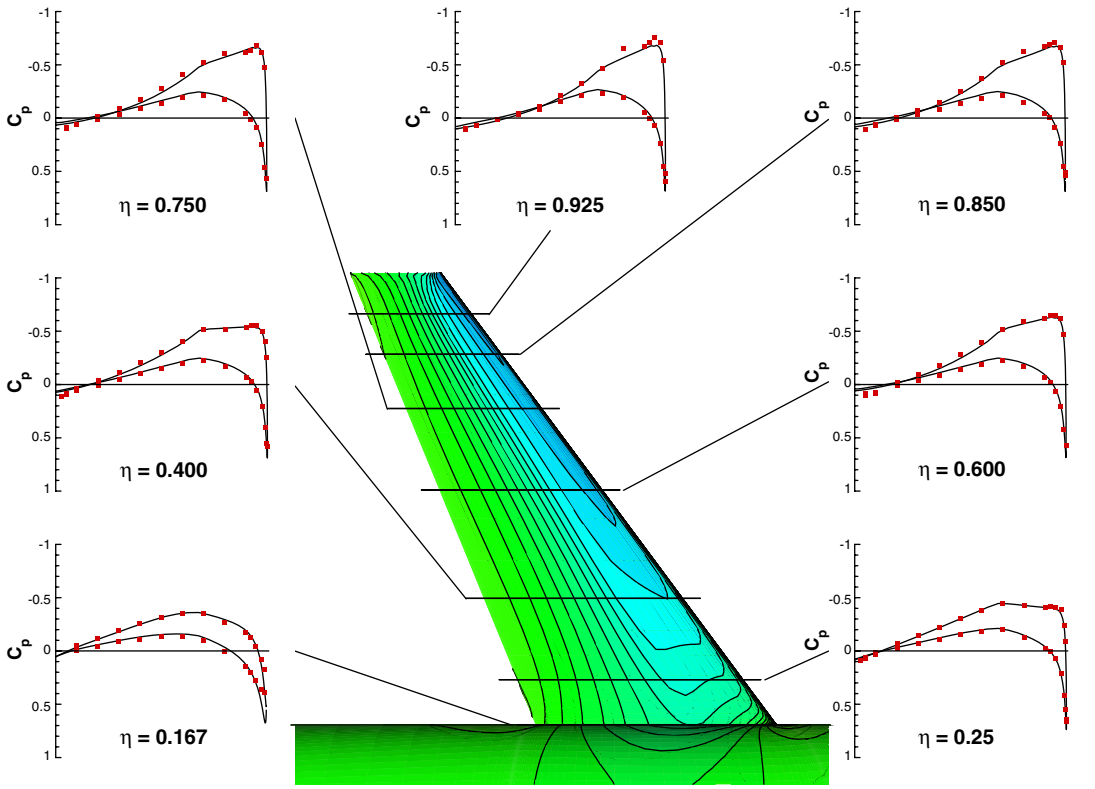

Figure 19. Surface pressure coefficient distributions on the wing of RAE wing body at $M = 0.8$, $Re = 1.0 \times 10^6$, $\alpha = 2^\circ$.

method for time integration, and Roe's approximate Riemann solver for the spatial discretization. Also, the effect of the turbulent kinetic energy contributions to the state equation and to the energy equation on the stability behaviour is considered. Von Neumann analysis and the numerical computations show that the stability characteristics of both coupling methods are identical when the turbulent kinetic energy contribution is ignored, and that the effects of the turbulent kinetic energy contribution on the stability characteristics in both coupling methods are negligible.

APPENDIX A

The inviscid Jacobian matrix of the coupled system is given by

$$\mathbf{K} = \frac{\partial \mathbf{F}}{\partial \mathbf{Q}} = \left[\begin{array}{c|c} \mathbf{K}^{\mathrm{ns}} & \mathbf{K}^{u} \\ \hline \mathbf{K}^{d} & \mathbf{K}^{q\omega} \end{array}\right]$$

$$= \left[\begin{array}{cccc|cc} 0 & n_x & n_y & 0 & 0 & 0 \\ (\gamma-1)n_x\bar{Q}-u_nu & u_n-(\gamma-2)n_xu & n_yu-(\gamma-1)n_xv & (\gamma-1)n_x & \phi n_x & 0 \\ (\gamma-1)n_y\bar{Q}-u_nv & n_xv-(\gamma-1)n_yu & u_n-(\gamma-2)n_yv & (\gamma-1)n_y & \phi n_y & 0 \\ \left\{2(\gamma-1)-\dfrac{\gamma e}{\rho}\right\}u_n & hn_x-(\gamma-1)u_nu & hn_y-(\gamma-1)u_nv & \gamma u_n & \phi u_n & 0 \\ \hline qu_n & n_xq & n_yq & 0 & u_n & 0 \\ \omega u_n & n_x\omega & n_y\omega & 0 & 0 & u_n \end{array}\right] \tag{A1}$$

where $\phi = -2C(\gamma-1)\zeta q$.

Here the eigenvalues of the inviscid Jacobian matrix are found to be

$$\mathbf{\Lambda} = \mathrm{diag}\{u_n \;\; u_n \;\; u_n + c \;\; u_n - c \,|\, u_n \;\; u_n\} \tag{A2}$$

where the speed of sound is defined by $c = \sqrt{\gamma(R + \zeta\frac{2}{3}(k/T))T}$. The first four eigenvalues are originated from the Navier–Stokes equations, while the latter two come from the q–ω turbulence model equations.

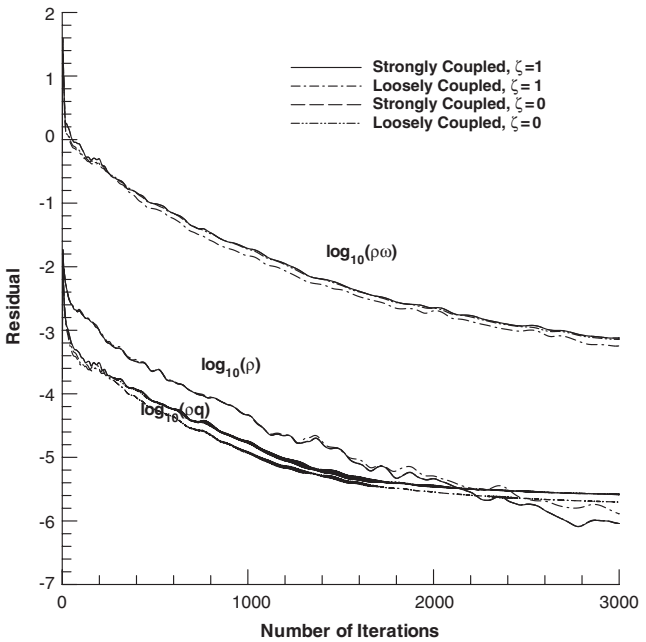

Figure 20. Comparison of the convergence histories of the strongly and the loosely coupled methods for flow over the RAE wing body at $M = 0.8$, $Re = 1.0 \times 10^6$, $\alpha = 2^\circ$.

The viscous Jacobian matrix can be found via the chain rule,

$$\left.\frac{\partial \mathbf{F}_v}{\partial \mathbf{Q}_{i+1}}\right|_{i+1/2} = \left.\frac{\partial \mathbf{F}_v}{\partial \mathbf{Q}_x}\frac{\partial \mathbf{Q}_x}{\partial \mathbf{Q}_{i+1}} + \frac{\partial \mathbf{F}_v}{\partial \mathbf{Q}_y}\frac{\partial \mathbf{Q}_y}{\partial \mathbf{Q}_{i+1}}\right|_{i+1/2} \tag{A3}$$

The terms like $\partial \mathbf{F}_v/\partial \mathbf{Q}_x$ and $\partial \mathbf{F}_v/\partial \mathbf{Q}_y$ are independent of the discretization scheme and can be found from Reference [4]. On the other hand, $\partial \mathbf{Q}_x/\partial \mathbf{Q}_{i+1}|_{i+1/2}$ and $\partial \mathbf{Q}_y/\partial \mathbf{Q}_{i+1}|_{i+1/2}$ can be obtained by directly differentiating the finite volume approximation of Equation (31). The resulting viscous Jacobian can be written as

$$\mathbf{K}_v = \frac{\partial \mathbf{F}_v}{\partial \mathbf{Q}} = \left[\begin{array}{c|c} \mathbf{K}_v^{\mathrm{ns}} & \mathbf{K}_v^{u} \\ \hline \mathbf{K}_v^{d} & \mathbf{K}_v^{q\omega} \end{array}\right]$$

$$= \left[\begin{array}{cccc|cc} 0 & 0 & 0 & 0 & 0 & 0 \\ -\dfrac{\mu_T}{\rho}(\alpha_{11}u - \alpha_{21}v) & \dfrac{\mu_T}{\rho}\alpha_{11} & -\dfrac{\mu_T}{\rho}\alpha_{21} & 0 & 0 & 0 \\ \dfrac{\mu_T}{\rho}(\alpha_{12}u - \alpha_{22}v) & -\dfrac{\mu_T}{\rho}\alpha_{12} & \dfrac{\mu_T}{\rho}\alpha_{22} & 0 & 0 & 0 \\ a_{41} & a_{42} & a_{43} & a_{44} & a_{45} & 0 \\ \hline -\dfrac{k_q\alpha_0}{\rho}q & 0 & 0 & 0 & \dfrac{k_q\alpha_0}{\rho} & 0 \\ -\dfrac{k_\omega\alpha_0}{\rho}\omega & 0 & 0 & 0 & 0 & \dfrac{k_\omega\alpha_0}{\rho} \end{array}\right] \tag{A4}$$

where

$$a_{41} = -a_{42}u - a_{43}v - a_{44}\frac{e}{\rho} - a_{45}q, \qquad a_{42} = (a_{22} - a_{44})u + a_{32}v$$

$$a_{43} = a_{23}u + (a_{33} - a_{44})v, \qquad a_{44} = \frac{(\gamma - 1)\alpha_0 k_T}{\rho}, \quad a_{45} = -2a_{44}q\zeta$$

The coefficients in the above equations depend on the geometry of computational cell, and are given by

$$\alpha_0 = \frac{\Delta s^2}{V}, \quad \alpha_{11} = \frac{\Delta S^2}{V}\left(\frac{4}{3}n_x^2 + n_y^2\right), \quad \alpha_{22} = \frac{\Delta S^2}{V}\left(n_x^2 + \frac{4}{3}n_y^2\right),$$

$$\alpha_{12} = a_{21} = -\frac{\Delta S^2}{3V}n_x n_y \tag{A5}$$

The eigenvalues of the viscous Jacobian matrix are found to be

$$\mathbf{\Lambda}_v = \frac{\Delta S^2}{V}\,\mathrm{diag}\left\{0 \;\; \frac{\mu_T}{\rho} \;\; \frac{4\mu_T}{3\rho} \;\; \frac{\gamma k_T}{\rho C_p} \;\middle|\; \frac{k_q}{\rho} \;\; \frac{k_\omega}{\rho}\right\} \tag{A6}$$

The Jacobian matrix for the source terms are found to be as

$$\mathbf{D} = \frac{\partial \mathbf{S}_{q\omega}}{\partial \mathbf{Q}} = \left[\begin{array}{cccc|cc} 0 & 0 & 0 & 0 & 0 & 0 \\ 0 & 0 & 0 & 0 & 0 & 0 \\ 0 & 0 & 0 & 0 & 0 & 0 \\ 0 & 0 & 0 & 0 & 0 & 0 \\ \hline C_{q1}\left(\dfrac{\mu_t S}{q} + \omega q\right) & 0 & 0 & 0 & C_{q1}\left(\dfrac{\mu_t S}{q^2} - \dfrac{2D}{3} - \omega\right) & -C_{q1}\left(\dfrac{\mu_t S}{q\omega} + q\right) \\ C_{\omega 1} C_\mu S + C_{\omega 2}\omega^2 & 0 & 0 & 0 & 0 & -C_{\omega 1} C_{\omega 3} D - 2C_{\omega 2}\omega \end{array}\right] \tag{A7}$$

However, as noted in the numerical method section, only destruction terms are treated implicitly. Then the Jacobian matrix for the source terms becomes

$$\mathbf{D} = \frac{\partial \mathbf{S}_{q\omega}}{\partial \mathbf{Q}} = \left[\begin{array}{cccc|cc} 0 & 0 & 0 & 0 & 0 & 0 \\ 0 & 0 & 0 & 0 & 0 & 0 \\ 0 & 0 & 0 & 0 & 0 & 0 \\ 0 & 0 & 0 & 0 & 0 & 0 \\ \hline C_{q1}\omega q & 0 & 0 & 0 & -C_{q1}\omega & -C_{q1} q \\ C_{\omega 2}\omega^2 & 0 & 0 & 0 & 0 & -2C_{\omega 2}\omega \end{array}\right] \tag{A8}$$

ACKNOWLEDGEMENTS

The authors would like to thank Prof. Yun-Ho Choi of Ajou University for the valuable discussions. The work was supported by Korea Science and Engineering Foundation under the grant number R01-2003-000-10744-0.

REFERENCES

1. Kunz RF, Lakshminarayana B. Stability of explicit Navier–Stokes procedures using k–ε and k–ε/algebraic Reynolds stress turbulence models. *Journal of Computational Physics* 1992; **103**.
2. Lui F, Zheng X. A strongly coupled time-marching method for solving the Navier–Stokes and k–ω turbulent model equations with multigrid. *Journal of Computational Physics* 1994; **128**.
3. Barakos G, Drikakis D. Implicit unfactored implementation of two-equation turbulence models in compressible Navier–Stokes methods. *International Journal for Numerical Methods in Fluids* 1998; **28**:73–94.
4. Venkateswaran S, Merkle CL. *Analysis of Preconditioning Methods for the Euler and Navier–Stokes Equations*. Lecture Note of Von Karman Institute Lecture Series, March, 1999.
5. Coakley TJ. A compressible Navier–Stokes code for turbulent flow modeling. *NASA TM 85899*, 1984.
6. Kim CS, Kim C, Rho OH. Parallel computations of high-lift airfoil flows using two-equation turbulence models. *AIAA Journal* 2000; **38**:1360–1369.
7. Ilinca F, Hetu J-F, Pelletier D. A single formulation and finite element algorithm: a tool for comparing two-equation models of turbulence. *AIAA Paper 97-1863*, 1997.

8. Lee S, Dulikravich G. Magnetohydrodynamic steady flow computations in three dimensions. *International Journal for Numerical Methods in Fluids* 1991; **13**:917–936.
9. Coakley TJ, Huang PG. Turbulence modeling for high speed flows. *AIAA Paper 92-0436*, 1992.
10. Hirsch C. *Numerical Computation of Internal and External Flows*, vol. I, II. Wiley: New York, 1990.
11. Jongen T, Marx YP. Design of an unconditionally stable, positive scheme for the k–ε and two-layer turbulence models. *Computers and Fluids* 1997; **26**(5):469–487.
12. Kwon O, Hah C. Solution of the 3-D Navier–Stokes equations with a two-equation turbulence model on unstructured meshes applied to turbomachinery. *AIAA Paper 94-1833*, 1994.
13. Thakur S, Wright J, Shyy W, Liu J, Ouyang H, Thi Vu T. Development of pressure-based composite multigrid methods for complex fluid flows. *Progress in Aerospace Sciences* 1996; **32**:313–375.
14. Cullen CG. *Matrices and Linear Transformations* (2nd edn). Addison-Wesley Publishing Co.: New York, 1972.
15. Cook PH, McDonald MA, Firmin MCP. Aerofoil RAE 2822 pressure distributions and boundary layer and wake measurement. *AGARD Advisory Report No. 138*, 1979.
16. Schmitt V, Charpin F. Pressure distributions on the ONERA-M6-Wing at transonic Mach numbers. *AGARD Advisory Report No. 138*, 1979.
17. Treadgold DA, Jones AF, Wilson KW. Pressure distribution measured in the RAE 8 ft $\times$ 6 ft transonic wind tunnel on RAE Wing 'A' in combination with an axi-symmetric body at Mach number of 0.4, 0.8 and 0.9. *AGARD Advisory Report No. 138*, 1979.

